

## Article

# Deformation Termination of the Kanggur Ductile Shear Zone in Eastern Tianshan, NW China: Insights from U-Pb Dating of Zircon and Apatite

Ping Li <sup>1,2</sup> , Ting Liang <sup>1,\*</sup>, Tong-Yang Zhao <sup>2</sup>, Yong-Gang Feng <sup>1</sup>, Gang Chen <sup>2</sup> and Zhi-Xin Zhu <sup>2</sup>

<sup>1</sup> School of Earth Science and Resources, Chang'an University, Xi'an 710054, China

<sup>2</sup> Geological Survey Academy of Xinjiang, Urumqi 830000, China

\* Correspondence: liangt@chd.edu.cn

**Abstract:** The Kanggur ductile shear zone (KDSZ), located in the south margin of the Central Asia Orogenic Belt (CAOB), plays a critical role in the tectonic evolution and mineralization in eastern Tianshan. Although different isotopic chronologies have been reported, the termination of the KDSZ deformation remains controversial. Here, we provide new data obtained by U-Pb dating of zircon and apatite from Huangshandong synkinematic granite (HSG) and Huludong deformed granite (HDG) to constrain the termination of the KDSZ deformation. The U-Pb age of apatite from HSG ( $249.1 \pm 1.8$  Ma) is identical to that of zircon ( $256.5 \pm 2.1$  Ma) within the error range. In contrast, the U-Pb age of apatite from HDG ( $248.1 \pm 4.0$  Ma) is significantly younger than that of zircon ( $347.3 \pm 2.5$  Ma). The HDG and HDG have the geochemical characteristics of I-type granites petrogenesis, including high SiO<sub>2</sub> (up to 75.47%), high alkaline (K<sub>2</sub>O + Na<sub>2</sub>O = 6.39%–8.05%), low FeO<sup>T</sup>/MgO (2.4–3.4), and peraluminous (A/CNK = 1.01–1.08). Combined with previous Sr-Nd isotope compositions, the positive zircon  $\epsilon$ Hf(t) values and  $T_{DM2}$  ages indicate that the ca. 347 Ma HDG originated from the re-melting of juvenile crust crustal-derived magma in a volcanic arc environment during the northward subduction of the Kanggur oceanic basin, and the ca. 257 Ma HSG originated from the partial melting of thickened juvenile crust in a post-collisional environment. Although trace elements of zircon show typical magmatic characteristics, apatite does not. With the presence of distinct major and trace elements in apatite, the apatite from HSG is characterized by high Mn (>2500 ppm), slight enrichment in the middle rare earth elements (MREEs), and obvious negative Eu anomalies ( $\delta$ Eu = 0.09–0.21), indicating that it is related to magmatic apatite. In contrast, the apatite from HDG, with low Mn (<860 ppm), depleted light rare earth elements (LREEs), and variable Eu anomalies ( $\delta$ Eu = 0.30–1.34), demonstrated fluid metasomatism with metamorphic overprinting. Combined with the regional geology and published geochronology data, the HSG is interpreted to be derived from the magma experiencing cooling crystallization in the plastic state from 256.5 to 249.1 Ma, while the HDG is considered to have experienced metamorphism and deformation between 347.3 and 248.1 Ma. Owing to the relatively low closure temperature of the U-Pb isotopic system, the apatite U-Pb ages are interpreted as Early Triassic tectono-magmatism events, corresponding to the end of deformation of the KDSZ. This is inferred to be related to the continuous evolution of the Paleo-Asian Ocean in the Late Permian to Early Triassic.

**Keywords:** apatite U-Pb age; deformation termination; ductile shear zone; Early Triassic; in-suit trace elements



**Citation:** Li, P.; Liang, T.; Zhao, T.-Y.; Feng, Y.-G.; Chen, G.; Zhu, Z.-X. Deformation Termination of the Kanggur Ductile Shear Zone in Eastern Tianshan, NW China: Insights from U-Pb Dating of Zircon and Apatite. *Minerals* **2022**, *12*, 1284. <https://doi.org/10.3390/min12101284>

Academic Editor: Dominique Gasquet

Received: 1 September 2022

Accepted: 10 October 2022

Published: 13 October 2022

**Publisher's Note:** MDPI stays neutral with regard to jurisdictional claims in published maps and institutional affiliations.



**Copyright:** © 2022 by the authors. Licensee MDPI, Basel, Switzerland. This article is an open access article distributed under the terms and conditions of the Creative Commons Attribution (CC BY) license (<https://creativecommons.org/licenses/by/4.0/>).

## 1. Introduction

The Central Asia Orogenic Belt (CAOB), surrounded by the North China, Tarim, European, and Siberian cratons (Figure 1a), is a typical accretionary orogen [1,2]. Different levels and types of ductile shear zones were formed during convergence, subduction accretion, collision, and amalgamation related to the Paleo-Asian Ocean [2–7]. Eastern Tianshan, as

an important part of the CAOB, is famous for the Kangjur Ductile Shear Zone (KDSZ) and associated orogenic deposits. The KDSZ of eastern Tianshan is considered not only to control the mineralization of gold deposits [8], but also to modify those of nickel and copper deposits [9,10]. Notably, there are several synkinematic granites and deformed granites in the KDSZ, including the Kezertage, Huangshan, Huangshandong, and Huludong intermediate-to-felsic intrusive rocks [11–14]. The deformation behavior of such bodies is critical for understanding tectonic processes within the continental lithosphere [15]. Although the termination of the KDSZ deformation is constrained by structural mapping [16] and various isotope dating methods, terminated isotopic age is still controversial and has been suggested to be in the Early Permian [13,17,18], Middle Permian [19–21], Late Permian [18,20], Early Triassic [14], and Middle Triassic [22].

Zircon, as the most abundant accessory mineral within igneous rocks, is hardly reformed in a wide range of temperatures and pressures and is widely used for geochronology [23–25]. Furthermore, apatite,  $\text{Ca}_5(\text{PO}_4)_3(\text{F}, \text{Cl}, \text{OH})$ , is also commonly observed in different igneous rocks over a range of different geological processes [26,27]. It is increasingly used for ascertaining the tectonic event history as it is a supplement to the recorded information of zircon grains [15,28,29]. Apatite fission track (AFT) thermochronology was gradually developed into a well-established method for the analysis of tectonic thermal evolution history within a near-surface to 120 °C low-temperature window [30–32]. Owing to its unique structure and chemical behavior, apatite has also been applied in high-temperature thermochronology studies in recent years [31,33], including constraints on the shear zone deformation time [15,34] and the metallogenetic process of magmatic hydrothermal deposits [35–37]. As the U-Pb apatite system has a closure temperature of ca. 350–550 °C [31,38–41], it is even cooler when there is fluid involved [26,37,42,43]. Therefore, apatite provides a unique opportunity to date the deformation and metasomatism in ductile shear zones [15].

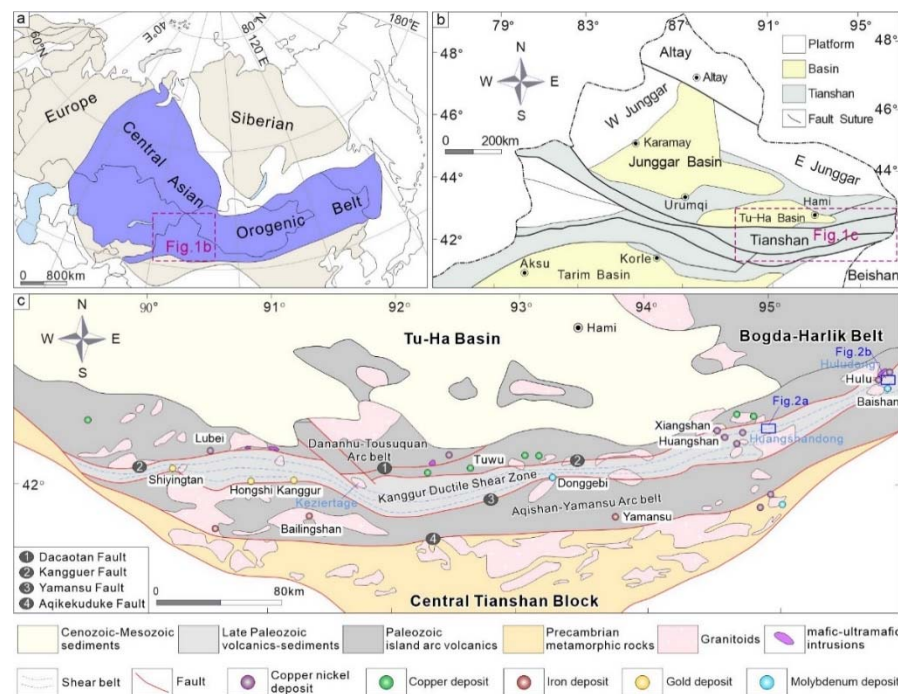


**Figure 1.** (a) Simplified map of the CAOB. (b) Tectonic framework in northern Xinjiang. (c) Simplified geological map of eastern Tianshan showing the distribution of representative deposits, modified from Li et al. [44].

In this study, we present the petrology, U-Pb ages of zircon and apatite, and major and trace element compositions of apatite of synkinematic and deformed granites to provide

new insights into the termination of the KDSZ deformation. These data add new constraints on the geodynamic setting of the KDSZ in the southern CAOB.

## 2. Geological Setting

Eastern Tianshan, located at the southern margin of the Tu-Ha basin (Figure 1b), has important metallogenic potentiality and hosts Cu-Ni-Au-Mo-Fe-Pb-Zn resources in Xinjiang, NW China (Figure 1c). The KDSZ in east–west direction is bound by the Kanggur dextral strike-slip shear fault and the Yamansu fault [12,45], with a scale that is ~500 km long and ~20 km wide. It is commonly subdivided into three tectonic units, namely the Dananhu–Tousuquan Belt, Jueluotage Belt (including Kanggur Ductile Shear Zone and Aqishan–Yamansu Arc), and Central Tianshan Block (Figure 1c) [44].

The strongly deformed strata of the KDSZ consist of the Lower Carboniferous Gandun Formation (flysch formation, e.g., tuffaceous siltstone, tuffaceous sandstone, and pyroclastic rock) and the Upper Carboniferous Wutongwozi Formation (pelagic sediments of deep-sea bathyal facies, e.g., bioclastic carbonate, siliceous rock, spilite, and tuffaceous siltstone), with massive Variscan–Indosinian granitoids, abundant Early Permian ultramafic–mafic intrusions, and tiny ophiolitic fragments [46–48]. Among them, the Permian synkinematic granite forming a lenticular tailing structure was produced by partial melting of the thickened juvenile lower crust in a post-collisional orogenic environment [2,47,49], whereas the Carboniferous granite that underwent deformation was likely derived from partial melting of metasomatized mantle wedge in a subduction-related arc environment [7,44]. Additionally, tight fold deformation occurred in the Carboniferous thin-layer clastic rocks, and σ-type rotated porphyroclasts developed in the mylonitized sandstone of the KDSZ [48,50,51]. All of the above deformation characteristics indicate that the KDSZ movements experienced compressive deformation, along with dextral strike slip [19,52]. In addition to the deformation, metamorphism is generally found in the KDSZ [50,51]. A series of important deposits occurred in the KDSZ, such as the orogenic gold deposits (e.g., Kanggur, Matoutan, and Shiyingtan deposits) [8], magmatic sulfide copper–nickel deposits (e.g., Lubei, Huangshan, Huangshandong, Huangshannan, Hulu, and Tulargen deposits) [9,53–55], porphyry molybdenum deposits (e.g., Baishan and Donggebi) [56,57], and pegmatite lithium–beryllite deposits (e.g., Jingerquan) [48,58].

The Dananhu–Tousuquan Belt, north of the KDSZ, is composed of Early Ordovician to Late Carboniferous volcanic and intrusive rocks, which host a series of significant porphyry copper deposits (e.g., Yuhai, Tuwu, and Fuxing) [59–61] and volcanic massive sulfide copper–zinc deposits (e.g., Huangtupo and Xiaorequanzi) [62,63]. From the Ordovician to Silurian, the rock assemblage transitioned from basalt and andesite to dacite and rhyolite, with tuff and subordinate limestone [64]. The Devonian strata generally consist of tuffaceous sandstones and siltstones with mafic to felsic volcanic rocks [65]. The Carboniferous strata are dominated by bimodal volcanic rocks, wherein the rocks of the Tuwu copper deposit are slightly deformed.

The Aqishan–Yamansu Belt, south of the KDSZ, consists of the Lower Carboniferous Yamansu Formation (shallow marine carbonate and terrigenous clastic formations with andesitic tuff) and the Upper Carboniferous Tugutubulake Formation (basaltic and andesitic pyroclastic rocks), along with granitic intrusive rocks and intermediate–basic dykes [66,67]. A series of iron deposits related to volcanism have been identified in this belt, including the Hongyuntan, Bailingshan, Heijianshan, Chilongfeng, and Yamansu deposits [68,69].

## 3. Petrology

Synkinematic and deformed granites subjected to dextral strike-slip shear are common in the KDSZ. The Huangshandong synkinematic granite (HSG) was emplaced into the Lower Carboniferous Gandun Formation and is approximately 8.5 km long and 2 km wide. Its lenticular shape indicates the presence of strong strike-slip extrusion stress in an uncooled plastic state (Figure 2a). The Huludong deformed granite (HDG) intruded

into the Lower Devonian Dananhu Formation with medium-grade metamorphism and deformation (Figure 2b).

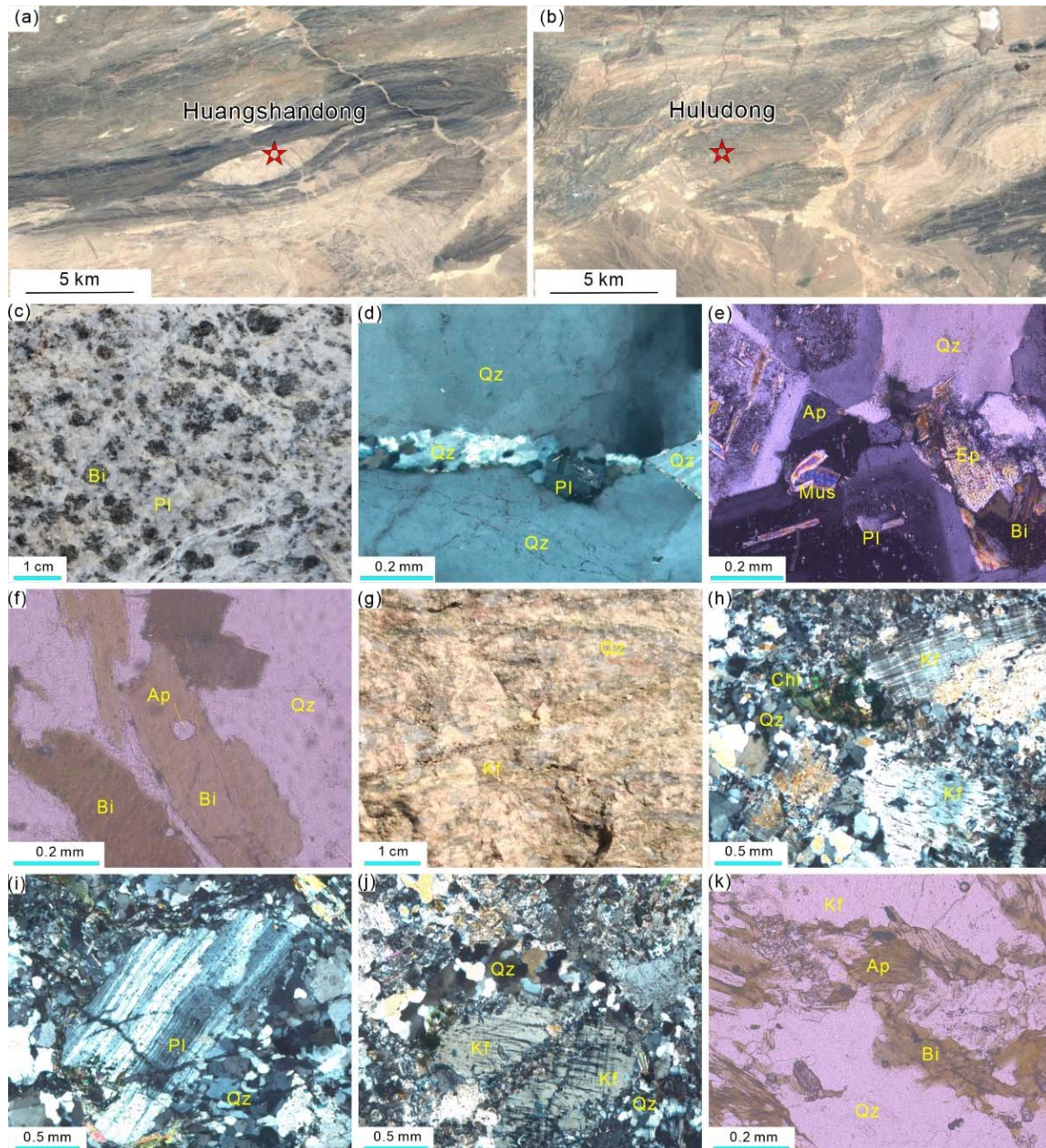


**Figure 2.** Typical features of the HSG and HDG. (a) The lenticular HSG. (b) The gneissic HDG. (c) Porphyry granodiorite of HSG. (d) Recrystallized quartz from HSG showing undulatory extinction in perpendicular polarized light. (e) Subhedral granular apatite from HSG associated with microcline with perpendicularly oriented quartz. (f) Granular apatite from HSG associated with biotite in plane polarized light. (g) Weakly oriented gneissic monzogranite of HDG. (h) Chlorite alteration and metasomatized K-feldspar from HDG with perpendicularly oriented quartz. (i) Deformed plagioclase from HDG surrounded by wave extinction quartz with perpendicularly oriented quartz. (j) Quartz with undulatory extinction around plagioclase with perpendicularly oriented quartz. (k) Subhedral granular apatite in plane polarized light. Mineral abbreviations: Q—quartz; Pl—plagioclase; Kf—K—feldspar; Bi—biotite; Mus—muscovite; Ep—epidote; Chl—chlorite; Ap—apatite.

### 3.1. Huangshandong Synkinematic Granite

The HSG, composed of granodiorite, is elongated lenticularly along the plane (Figure 2a) and may have experienced ductile deformation in the plastic state. Previous studies have identified that the HSG was emplaced in the Middle–Late Permian [70,71]. The granodiorite of HSG mainly comprises plagioclase (50%–60%), quartz (25–30%), K-feldspar (10%±), and minor biotite and muscovite (Figure 2c,e). Recrystallization occurs at the edge of the large-grain quartz, which displays wavy extinction (Figure 2d). Biotite is schistose, showing chloritization and epidotization (Figure 2e). The apatite is hypidiomorphic granular and distributed between biotite and plagioclase (Figure 2f).

### 3.2. Huludong Deformed Granite

The Early Carboniferous deformed granites have been reported to exist in many places of the KDSZ, for instance Knaggur, Jianshan, and Huludong [8]. The HDG, composed of monzogranite, has a gneissic structure and undergoes middle- and high-grade metamorphism and deformation (Figure 2g). The monzogranite of the HDG mainly comprises K-feldspar (35%±), plagioclase (30%±), quartz (25%±), and minor biotite (Figure 2h). Subsequently, K-feldspar and plagioclase formed porphyroclasts, and the quartz recrystallized to form a matrix (Figure 2i,j). The K-feldspar (0.15–3.0 mm) comprises microcline, with argillarization, chlorite, and epidotite alteration (Figure 2h). The plagioclase (0.12–2.0 mm) with agglomerated lamellae twins is obviously dislocated (Figure 2i). The quartz distributed around the microcline shows wavy extinction and recrystallization (Figure 2j). The biotite with slight deformation experienced chloritization and epidotization. The particle size of apatite is 0.02–0.12 mm, and the apatite is subhedral granular, distributed in biotite schistosity or wrapped in quartz (Figure 2k).

## 4. Analytical Methods

### 4.1. Zircon U-Pb Dating

Zircon and apatite grains were separated from the whole-rock samples using heavy liquid and magnetic techniques, hand-picked under a binocular microscope, and mounted in epoxy resin. The internal structure of the zircons (including zoning, structures, and fractures) was characterized by cathodoluminescence (CL) imaging using a Cameca electron microprobe (JSM-6510A from Japan) at Yujin Technology Co., Ltd. Trace element composition analysis and U-Pb dating of zircon were conducted by using an Agilent 7500a laser ablation system coupled with an iCAP RQ ICP-MS at Nanjing FocuMS Technology Co., Ltd. The analytical spot size, laser frequency, and energy density were 32  $\mu\text{m}$ , 5 Hz, and 6.5  $\text{J}/\text{cm}^2$ , respectively. The analytical drift of the U-Th-Pb isotope ratio was corrected using linear interpolation (with time) for every 10 analyses in accordance with variations in the standard zircon 91,500. Weighted mean calculations and concordia diagrams were produced using the ISOPLOT software [72]. In situ zircon trace element analyses were conducted on the same zircon grains that had been analyzed for U-Pb isotopes, and the analysis procedures and conditions were the same as those for the U-Pb isotopic analysis. The time-resolved spectra were processed offline using the ICP-MS DataCal software [73].

### 4.2. Apatite U-Pb Dating

Zircon U-Pb isotope analysis was carried out in-situ by using a NWR193 laser-ablation microprobe (Elemental Scientific Lasers LLC), attached to a Analytikjena M90 at Yan-duzhongshi Geological Analysis Laboratories Ltd.. The downhole fractionation, instrument drift, and mass bias correction factors for Pb/U ratios on apatite were calculated using two analyses on the primary (MAD2) [74] and secondary standard apatite: McClure Mt [75], Otter Lake [31,76] and Durango [77] analyzed at the beginning of the session and after every 10 unknown apatites using the same spot size and conditions as those used for the samples. The trace element contents of apatite were quantified using SRM610 as an external standard and  $^{44}\text{Ca}$  as the internal standard element assuming stoichiometric proportions.

Each analysis of the apatite began with a 20 s blank gas measurement followed by a further 40 s of analysis time after the laser was switched on. Apatite was sampled at 40  $\mu\text{m}$  spots using a laser at 8 Hz and a density of approximately 4 J/cm<sup>2</sup>. A flow of He carrier gas at a rate of 0.55 L/min carried the particles ablated by the laser out of the chamber to be mixed with Ar gas and subsequently carried to the plasma torch. Isotopes measured included <sup>31</sup>P, <sup>44</sup>Ca, <sup>140</sup>Ce, <sup>202</sup>Hg, <sup>204</sup>Pb, <sup>206</sup>Pb, <sup>207</sup>Pb, <sup>208</sup>Pb, <sup>232</sup>Th, and <sup>238</sup>U wherein each element was measured every 0.18 s with a longer counting time for Pb isotopes compared to the other elements. The data reduction used was based on the detailed method outlined by Meffre et al. [78] with an additional modification to correct for the small amount of common Pb present in the primary standard using the <sup>207</sup>Pb correction [79].

#### 4.3. Major and Trace Elements of Apatite

The major and trace elements of apatite were determined at Yanduzhonqshi Geological Analysis Laboratories Ltd. The major elements of apatite grains were determined using a JEOL JXA 8230 electron probe microanalyzer equipped with four wavelength-dispersive-type spectrometers. The operating conditions were as follows: 15 kV accelerating voltage, 20 nA beam current, and 5  $\mu\text{m}$  focused electron beam size. The standards used were as follows: apatite [F, P, Ca], corundum [Al], jadeite [Si, Na], CeP<sub>5</sub>O<sub>14</sub> (synthetic) [Ce], KNbO<sub>3</sub> (synthetic) [K], PbMoO<sub>4</sub> (synthetic) [Pb], U-Th-Pb (synthetic) [Th], LaP<sub>5</sub>O<sub>14</sub> (synthetic) [La], PrP<sub>5</sub>O<sub>14</sub> (synthetic) [Pr], NaCl (synthetic) [Cl], MnO (synthetic) [Mn], barite [S], uraninite [U], magnetite [Fe], olivine [Mg], and rutile [Ti]. The analytical reproducibility was within 2%. The trace elements in apatite were determined using LA-ICP-MS. LA-ICP-MS analysis of separated apatite grains was conducted using an Analytikjena M90 quadrupole ICPMS with a 193 nm NWR193 Ar-F excimer laser. An Agilent 7700× ICP-MS instrument with helium as the carrier gas was used to acquire the ion-signal intensities. The laser ablation spots were 25  $\mu\text{m}$  in diameter. The international standards NIST SRM 610 and NIST SRM 612 were used for the external calibration of the in situ apatite analysis. <sup>43</sup>Ca was used as the internal standard for the LA-ICP-MS calibration. Data reduction was conducted using the ICP-MS DataCal software [80].

#### 4.4. In Situ Hf Isotopic Dating

Zircon in situ Hf isotope analysis was conducted at Nanjing FocuMS Technology Co., Ltd. using a New Wave ArF 193 nm laser ablation system coupled to a Neptune Plus MC-ICP-MS. Analytical spots were located close to or on the top of the previous LA-ICP-MS analytical spots, with a beam diameter and laser repetition rate of 44  $\mu\text{m}$  and 8 Hz at 15 J/cm<sup>2</sup>, respectively. During the analysis, the standard 91,500 zircon, <sup>176</sup>Hf/<sup>177</sup>Hf = 0.282296  $\pm$  0.000008 (2 $\sigma$ ), was used for external standardization. The <sup>176</sup>Lu decay constant in the  $\varepsilon$ Hf(t) calculation was  $1.865 \times 10^{-11}\text{y}^{-1}$  [81]. The depleted mantle line was defined by present-day <sup>176</sup>Hf/<sup>177</sup>Hf = 0.28325 and <sup>176</sup>Hf/<sup>177</sup>Hf = 0.0384 [82]. The single-stage ( $T_{\text{DM}}$ ) and two-stage Hf model ages ( $T_{\text{DM2}}$ ) were calculated using the methods of Griffin et al. [82] and Griffin et al. [83], respectively.

#### 4.5. Major and Trace Elements of Granites

Whole-rock geochemical compositions were obtained at the Xinjiang Institute of Geology and Mineral Resources. The main elements were determined using a Philips PW2404X XRF and an Axios X-ray fluorescence spectrometer. Trace element compositions were determined using a Finnigan MAT HR-ICP-MS and NexION 300× after acid digestion of the samples in Teflon bombs.

### 5. Results

#### 5.1. Zircon U-Pb Ages

Two samples of HSG and HDG were dated using zircon U-Pb analysis. The LA-ICP-MS dating results are presented in Table 1; representative CL images of zircon grains from these rocks are shown in Figure 3. All the analyzed zircons are prismatic, euhedral, and

colorless, and most of them show oscillatory zoning patterns, which imply a magmatic origin. The analyzed zircons have variable U (38.2–298.8 ppm) and Th (12.7–160.4 ppm) contents, with Th/U ratios ranging from 0.15 to 0.71. Twenty-five zircon grains from HSG show a narrow range with  $^{206}\text{Pb}/^{238}\text{U}$  ages of 248.4 to 267.1 Ma, yielding a concordant age of  $256.6 \pm 1.1$  Ma (MSWD = 4.6; Figure 4a), with a weighted mean age of  $256.5 \pm 2.1$  Ma (MSWD = 0.89; Figure 4b). Twenty-three zircon grains from HDG show a narrow range with  $^{206}\text{Pb}/^{238}\text{U}$  ages of 337.6 to 358.8 Ma, yielding a concordant age of  $347.3 \pm 0.9$  Ma (MSWD = 1.2; Figure 4c), with a weighted mean age of  $347.3 \pm 2.5$  Ma (MSWD = 1.8; Figure 4d).

Results for apatite dating of HSG and HDG are presented in Table 2. Thirty apatite grains from HSG show a narrow range with  $^{207}\text{Pb}$ -corrected ages of 229.4 to 284.0 Ma, yielding a lower intercept age of  $249.2 \pm 3.5$  Ma (MSWD = 1.08; Figure 5a), with a weighted mean age of  $249.1 \pm 1.8$  Ma (MSWD = 0.97; Figure 5b). Twenty-nine apatite grains from HDG show a narrow range with  $^{207}\text{Pb}$ -corrected ages of 217.2 to 269.9 Ma, yielding a lower intercept age of  $247 \pm 11$  Ma (MSWD = 0.46; Figure 5c), with a weighted mean age of  $248.1 \pm 4.0$  Ma (MSWD = 0.68; Figure 5d).

### 5.2. Trace Element Composition of Zircon

A total of 45 analyses were conducted for zircon grains to estimate trace element composition in HSG and HDG, and the results are presented in Table 3. The zircon grains from HSG have low Ti (0.59–10.25 ppm, mean = 5.03 ppm) and Ta (0.15–1.06 ppm, mean = 0.35 ppm). In comparison, the zircon grains from HDG have high Ti (5.65–12.10 ppm, mean = 8.69 ppm) and Ta contents (0.51–0.67 ppm, mean = 0.56 ppm). The chondrite-normalized REE patterns of the zircon grains from both HSG and HDG show depleted LREEs, enriched HREEs, and weak negative Eu and large positive Ce anomalies (Figure 4a,c). Combined with oscillatory zoning, high Th/U ratios (>0.1), and identical REE patterns, zircons from both HSG and HDG show the characteristics of typical magmatic zircon [84,85].

### 5.3. Major and Trace Element Compositions of Apatite

A total of 38 analyses were conducted for apatite grains to estimate major and trace elements by electron probe microanalysis (EPMA) and LA-ICP-MS, respectively, and the results are presented in Tables 4 and 5. The apatite grains from HSG and HDG have similar CaO, P<sub>2</sub>O<sub>5</sub>, SiO<sub>2</sub>, and Cl contents, in the ranges of 53.17–55.83, 41.28–42.96, 0–0.26, and 0–0.08 wt.%, respectively. The apatite grains from HSG have high MnO (0.33–0.82 wt.%, average: 0.58 wt.%), FeO<sup>T</sup> (0.03–0.22 wt.%, average: 0.11 wt.%), and F contents (2.90–4.10 wt.%, average: 3.44 wt.%). In contrast, the apatite grains from the HDG have low MnO (0.04–0.15 wt.%, average: 0.09 wt.%), FeO<sup>T</sup> (0–0.05 wt.%, average: 0.02 wt.%), and F contents (1.89–4.15 wt.%, average: 2.87 wt.%).

The apatite grains from HSG have high Mn (2570–7960 ppm, mean = 6204.7 ppm) and Fe contents (1140–4770 ppm, mean = 2775.8 ppm). In contrast, the apatite grains from HDG have low Mn (493–854 ppm, mean = 692.5 ppm), Fe (226–928 ppm, mean = 469.9 ppm), and LREE contents (35–1315 ppm, mean = 279.1 ppm). The chondrite-normalized REE patterns of apatite grains from the HSG show enrichment in LREEs (1012–3168 ppm, mean = 1827.4 ppm) with obvious negative Eu anomalies ( $\delta\text{Eu} = 0.09$ –0.21). In comparison, the apatite grains from the HDG have variable total REEs ranging from 170.9 to 2442.6 ppm (mean = 879.9 ppm) and low LREE/HREE (0.2–1.2, mean = 0.5).

**Table 1.** LA-ICP-MS U-Pb data of zircon grains from HSG and HDG of the KDSZ.

Spot No.	Th (ppm)	U (ppm)	Th/U	Isotope Ratios						Ages (Ma)						Concordance
				$^{207}\text{Pb}/^{206}\text{Pb}$	1σ	$^{207}\text{Pb}/^{235}\text{U}$	1σ	$^{206}\text{Pb}/^{238}\text{U}$	1σ	$^{207}\text{Pb}/^{206}\text{Pb}$	1σ	$^{207}\text{Pb}/^{235}\text{U}$	1σ	$^{206}\text{Pb}/^{238}\text{U}$	1σ	
HSG																
20HSD-01	15.7	66.9	0.23	0.05537	0.00450	0.29879	0.02392	0.04019	0.00098	427.8	181.5	265.5	18.7	254.0	6.1	95%
20HSD-02	61.0	298.8	0.20	0.05022	0.00155	0.28373	0.00993	0.04085	0.00082	205.6	72.2	253.6	7.9	258.1	5.1	98%
20HSD-03	18.9	74.9	0.25	0.05167	0.00356	0.28323	0.02103	0.03985	0.00093	333.4	157.4	253.2	16.6	251.9	5.8	99%
20HSD-04	20.1	106.4	0.19	0.05407	0.00315	0.29180	0.01783	0.03977	0.00098	372.3	131.5	260.0	14.0	251.4	6.1	96%
20HSD-05	41.3	119.7	0.35	0.05357	0.00286	0.29989	0.01621	0.04022	0.00086	353.8	125.0	266.3	12.7	254.2	5.3	95%
20HSD-06	38.7	132.3	0.29	0.05463	0.00263	0.31091	0.01343	0.04230	0.00079	398.2	107.4	274.9	10.4	267.1	4.9	97%
20HSD-07	18.0	41.8	0.43	0.05475	0.00381	0.29885	0.02001	0.04098	0.00109	466.7	155.5	265.5	15.6	258.9	6.8	97%
20HSD-08	41.7	115.6	0.36	0.05333	0.00291	0.28544	0.01445	0.03929	0.00071	342.7	124.1	255.0	11.4	248.4	4.4	97%
20HSD-09	28.0	96.7	0.29	0.05047	0.00241	0.28558	0.01501	0.04078	0.00088	216.7	111.1	255.1	11.9	257.7	5.4	98%
20HSD-10	34.2	102.8	0.33	0.05200	0.00312	0.29050	0.01733	0.04019	0.00079	287.1	137.0	259.0	13.6	254.0	4.9	98%
20HSD-11	45.1	95.7	0.47	0.05391	0.00237	0.30509	0.01357	0.04112	0.00082	368.6	100.0	270.4	10.6	259.8	5.0	96%
20HSD-12	12.7	44.9	0.28	0.05242	0.00328	0.29655	0.02013	0.04125	0.00104	305.6	142.6	263.7	15.8	260.6	6.4	98%
20HSD-13	22.1	53.8	0.41	0.05298	0.00305	0.30228	0.01735	0.04100	0.00098	327.8	131.5	268.2	13.5	259.0	6.1	96%
20HSD-14	54.6	198.7	0.27	0.05261	0.00180	0.29914	0.01061	0.04126	0.00068	322.3	77.8	265.7	8.3	260.6	4.2	98%
20HSD-16	14.4	38.2	0.38	0.05646	0.00556	0.29700	0.02358	0.04105	0.00109	477.8	220.3	264.1	18.5	259.3	6.8	98%
20HSD-18	27.9	69.1	0.40	0.05567	0.00327	0.31529	0.02015	0.04157	0.00110	438.9	131.5	278.3	15.6	262.5	6.8	94%
20HSD-19	65.6	119.8	0.55	0.05313	0.00248	0.30033	0.01530	0.04028	0.00075	344.5	100.9	266.7	11.9	254.6	4.6	95%
20HSD-20	71.2	139.4	0.51	0.05150	0.00221	0.29278	0.01528	0.04098	0.00109	264.9	102.8	260.7	12.0	258.9	6.7	99%
20HSD-21	30.9	77.2	0.40	0.05307	0.00295	0.29623	0.01584	0.04140	0.00091	331.5	121.3	263.4	12.4	261.5	5.7	99%
20HSD-23	29.8	72.1	0.41	0.05270	0.00272	0.29648	0.01503	0.04103	0.00083	316.7	116.7	263.6	11.8	259.2	5.2	98%
20HSD-24	31.7	80.3	0.40	0.05192	0.00279	0.28666	0.01629	0.04046	0.00090	283.4	156.5	255.9	12.9	255.7	5.6	99%
20HSD-25	29.4	138.1	0.21	0.05177	0.00263	0.27838	0.01389	0.03937	0.00069	276.0	116.7	249.4	11.0	249.0	4.3	99%
20HSD-26	47.0	79.8	0.59	0.05278	0.00300	0.29014	0.01670	0.03956	0.00070	320.4	129.6	258.7	13.1	250.1	4.3	96%
20HSD-28	14.7	95.9	0.15	0.05519	0.00310	0.29758	0.01555	0.04064	0.00093	420.4	119.4	264.5	12.2	256.8	5.8	97%
20HSD-30	27.8	136.3	0.20	0.05303	0.00275	0.30393	0.01644	0.04193	0.00103	331.5	116.7	269.5	12.8	264.8	6.4	98%
HDG																
20HLD-01	56.4	130.7	0.43	0.05485	0.00191	0.40944	0.01384	0.05474	0.00070	405.6	77.8	348.5	10.0	343.6	4.3	98%
20HLD-03	79.8	175.2	0.46	0.05240	0.00156	0.39822	0.01139	0.05536	0.00063	301.9	66.7	340.4	8.3	347.3	3.9	97%
20HLD-04	35.3	78.4	0.45	0.05398	0.00196	0.39407	0.01367	0.05379	0.00068	368.6	81.5	337.3	10.0	337.7	4.2	99%
20HLD-05	23.4	50.1	0.47	0.05590	0.00246	0.41088	0.01735	0.05377	0.00080	455.6	98.1	349.5	12.5	337.6	4.9	96%
20HLD-06	89.7	133.0	0.67	0.05436	0.00158	0.42099	0.01210	0.05645	0.00070	387.1	64.8	356.8	8.6	354.0	4.2	99%
20HLD-07	40.7	79.3	0.51	0.05753	0.00238	0.42689	0.01704	0.05450	0.00087	522.3	97.2	361.0	12.1	342.1	5.3	94%
20HLD-08	41.8	82.8	0.50	0.05537	0.00244	0.41553	0.01839	0.05501	0.00076	427.8	100.0	352.8	13.2	345.2	4.6	97%
20HLD-09	35.8	83.0	0.43	0.05442	0.00226	0.39736	0.01552	0.05444	0.00069	387.1	89.8	339.7	11.3	341.7	4.2	99%
20HLD-10	30.5	66.3	0.46	0.05494	0.00246	0.41322	0.01731	0.05614	0.00083	409.3	100.0	351.2	12.4	352.1	5.1	99%
20HLD-12	55.9	106.4	0.53	0.05409	0.00175	0.41412	0.01322	0.05604	0.00065	376.0	76.8	351.8	9.5	351.5	4.0	99%
20HLD-13	40.1	84.0	0.48	0.05262	0.00193	0.40693	0.01488	0.05666	0.00071	322.3	80.5	346.7	10.7	355.3	4.3	97%
20HLD-14	32.5	67.3	0.48	0.05652	0.00262	0.41128	0.01850	0.05418	0.00080	472.3	101.8	349.8	13.3	340.1	4.9	97%
20HLD-15	36.2	81.6	0.44	0.05563	0.00216	0.42233	0.01666	0.05496	0.00066	438.9	85.2	357.7	11.9	344.9	4.0	96%
20HLD-16	36.6	72.9	0.50	0.05539	0.00233	0.41998	0.01756	0.05569	0.00080	427.8	94.4	356.0	12.6	349.4	4.9	98%
20HLD-17	70.0	112.0	0.62	0.05555	0.00192	0.42132	0.01427	0.05599	0.00068	435.2	77.8	357.0	10.2	351.2	4.2	98%
20HLD-18	69.7	117.3	0.59	0.05592	0.00178	0.41594	0.01295	0.05486	0.00064	450.0	72.2	353.1	9.3	344.3	3.9	97%
20HLD-19	50.8	104.1	0.49	0.05322	0.00196	0.41120	0.01402	0.05723	0.00068	338.9	83.3	349.7	10.1	358.8	4.1	97%
20HLD-20	28.9	64.8	0.45	0.05371	0.00236	0.39511	0.01630	0.05516	0.00082	366.7	98.1	338.1	11.9	346.1	5.0	97%
20HLD-21	43.7	77.5	0.56	0.05434	0.00211	0.40862	0.01522	0.05538	0.00071	383.4	91.7	347.9	11.0	347.5	4.3	99%
20HLD-22	33.9	76.3	0.44	0.05601	0.00230	0.41306	0.01580	0.05441	0.00070	453.8	88.0	351.1	11.4	341.6	4.3	97%
20HLD-23	54.1	104.6	0.52	0.05674	0.00194	0.42703	0.01472	0.05516	0.00069	479.7	43.5	361.1	10.5	346.1	4.2	95%
20HLD-24	160.4	225.6	0.71	0.05255	0.00128	0.40967	0.01015	0.05653	0.00055	309.3	55.6	348.6	7.3	354.5	3.3	98%
20HLD-25	47.4	79.6	0.60	0.05510	0.00203	0.41089	0.01463	0.05517	0.00079	416.7	83.3	349.5	10.5	346.2	4.8	99%

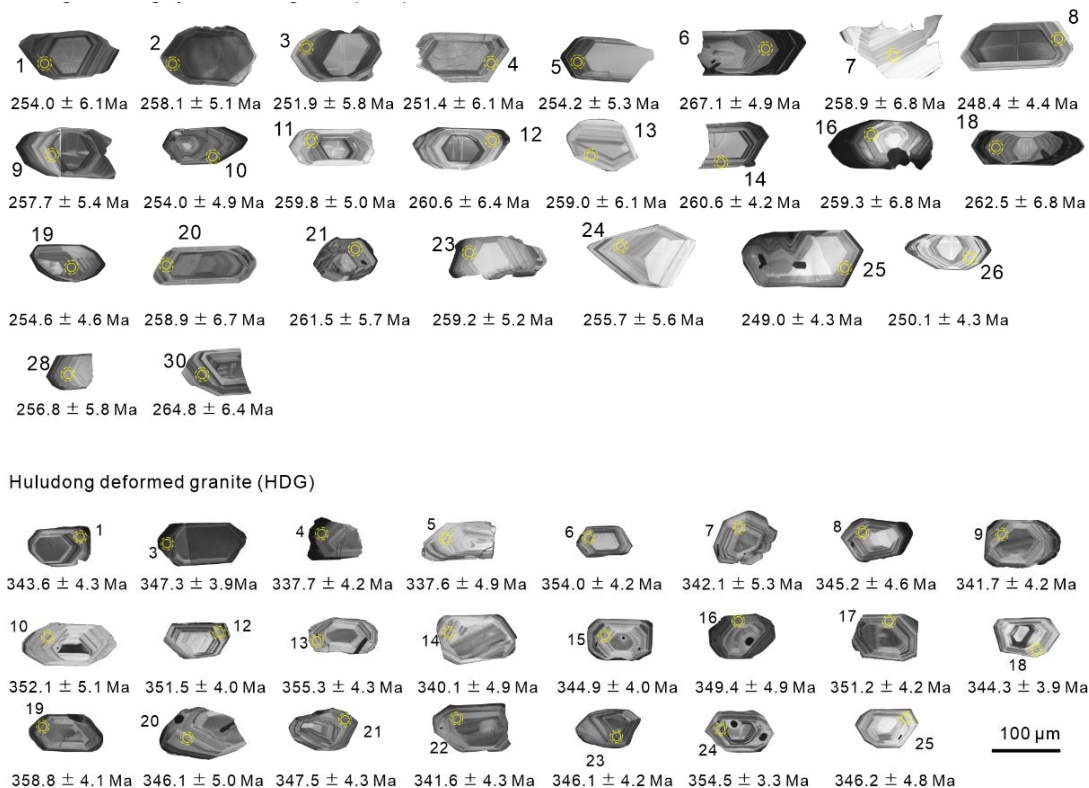


**Figure 3.** Cathodoluminescence (CL) images of representative zircons from the HSG and HDG.

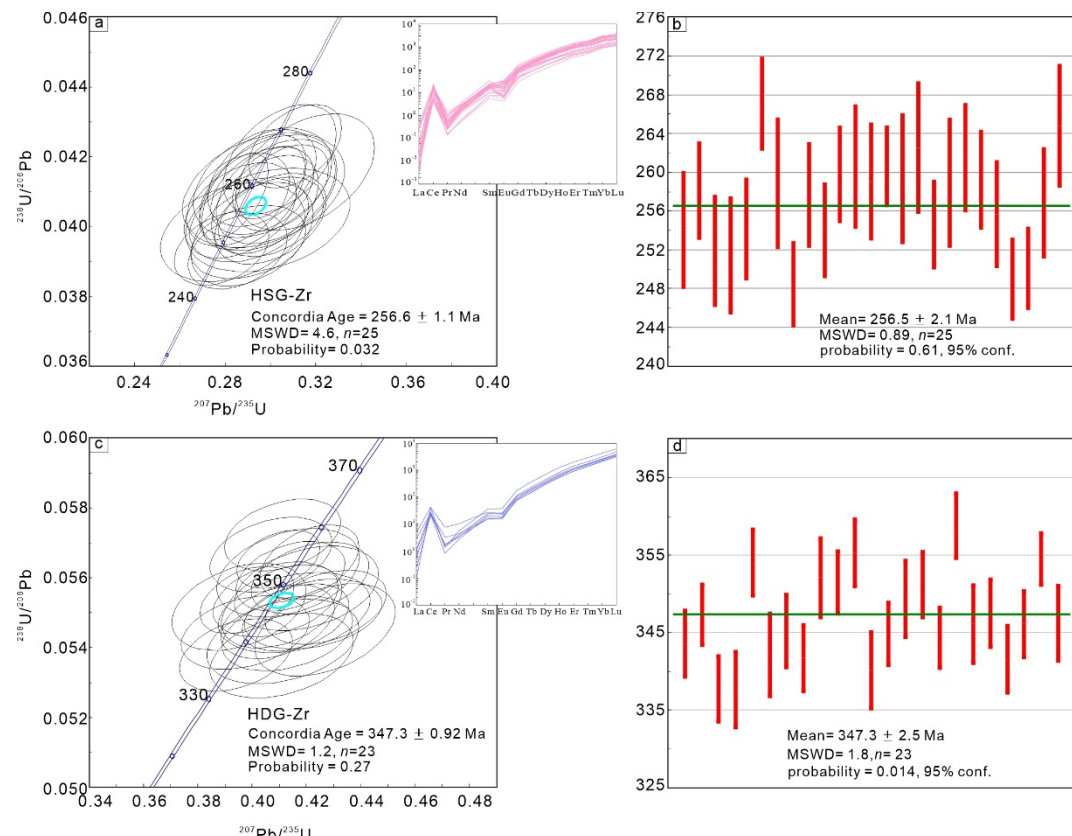


**Figure 4.** (a) U-Pb concordia diagram of the zircons from the HSG. (b) Weighted mean  $^{206}\text{Pb}/^{238}\text{U}$  age of the zircons from the HSG. (c) U-Pb concordia diagram of the zircons from the HDG. (d) Weighted mean  $^{206}\text{Pb}/^{238}\text{U}$  age of the zircons from the HDG.5.2. Apatite U-Pb Ages.

**Table 2.** LA-ICP-MS U-Th-Pb data of apatite grains from HSG and HDG of the KDSZ.

Spot No.	U	Th	Pb	Isotope Ratios						$f_{206}^{204}$ %	Ages (Ma)							
	ppm	ppm	ppm	$^{207}\text{Pb}/^{206}\text{Pb}$	$\pm\sigma$	$^{207}\text{Pb}/^{235}\text{U}$	$\pm\sigma$	$^{206}\text{Pb}/^{238}\text{U}$	$\pm\sigma$		$^{207}\text{Pb}/^{206}\text{Pb}$	$\pm\sigma$	$^{207}\text{Pb}/^{235}\text{U}$	$\pm\sigma$	$^{206}\text{Pb}/^{238}\text{U}$	$\pm\sigma$	$^{207}\text{Pb-corr.}$	$\pm\sigma$
HSG																		
20HSD-01	131.09	0.11	8.33	0.12623	0.00367	0.77388	0.02453	0.04410	0.00084	0.09	2046.1	51.4	582.0	14.0	278.2	5.2	252.3	5.0
20HSD-02	20.09	1.21	3.07	0.38557	0.00812	3.75370	0.09713	0.07005	0.00107	0.42	3853.7	31.8	1582.9	20.7	436.5	6.4	256.2	6.1
20HSD-03	23.54	1.46	3.26	0.35342	0.00763	3.02761	0.06628	0.06227	0.00089	0.38	3721.8	32.9	1414.6	16.7	389.4	5.4	245.6	5.2
20HSD-04	22.63	1.75	2.96	0.32431	0.00725	2.73325	0.06319	0.06147	0.00094	0.34	3590.4	34.3	1337.5	17.2	384.6	5.7	256.9	5.3
20HSD-05	69.16	0.93	5.43	0.19362	0.00313	1.27268	0.02111	0.04781	0.00056	0.18	2773.2	26.5	833.6	9.4	301.1	3.4	248.7	3.2
20HSD-06	82.71	0.73	5.88	0.16399	0.00225	1.04088	0.01534	0.04618	0.00055	0.14	2497.2	23.1	724.4	7.6	291.0	3.4	251.0	3.1
20HSD-07	114.91	1.12	7.13	0.12941	0.00503	0.77851	0.02723	0.04390	0.00095	0.10	2090.0	68.4	584.6	15.5	277.0	5.9	250.7	5.6
20HSD-08	35.26	0.69	3.19	0.24451	0.00414	1.66734	0.02843	0.04995	0.00067	0.24	3149.6	26.9	996.2	10.8	314.2	4.1	240.6	3.7
20HSD-09	1.76	0.03	3.72	0.25783	0.00610	1.86368	0.04409	0.05240	0.00077	0.26	3233.5	37.3	1068.3	15.6	329.2	4.7	245.8	4.3
20HSD-10	61.79	2.73	5.03	0.20805	0.00344	1.37342	0.02435	0.04821	0.00057	0.19	2890.4	26.9	877.6	10.4	303.5	3.5	245.7	3.3
20HSD-11	46.74	0.20	3.97	0.20306	0.00841	1.43364	0.04988	0.05149	0.00124	0.19	2850.9	67.5	903.1	20.8	323.6	7.6	264.1	6.9
20HSD-12	19.37	0.51	2.47	0.32951	0.01409	2.62313	0.12691	0.05801	0.00163	0.35	3614.8	65.5	1307.1	35.6	363.5	9.9	240.1	9.2
20HSD-13	44.48	0.34	4.27	0.24565	0.00392	1.78172	0.03738	0.05258	0.00077	0.24	3157.0	25.4	1038.8	13.6	330.4	4.7	251.7	4.3
20HSD-14	16.54	2.29	2.98	0.41961	0.00742	4.18075	0.08373	0.07304	0.00130	0.45	3980.9	26.5	1670.3	16.4	454.5	7.8	251.9	7.2
20HSD-15	81.04	0.90	5.91	0.17778	0.00244	1.15330	0.02272	0.04678	0.00068	0.16	2632.3	22.8	778.8	10.7	294.7	4.2	248.6	3.8
20HSD-16	69.09	1.04	5.34	0.18467	0.00267	1.24104	0.02537	0.04854	0.00076	0.17	2695.3	23.9	819.4	11.5	305.6	4.7	255.4	4.3
20HSD-17	13.43	6.53	3.07	0.47338	0.01003	6.02486	0.18570	0.09092	0.00207	0.54	4160.4	31.4	1979.4	26.8	560.9	12.3	266.3	10.4
20HSD-18	42.05	1.67	4.03	0.24638	0.00436	1.80278	0.04485	0.05251	0.00095	0.25	3161.7	28.1	1046.5	16.2	329.9	5.8	250.0	5.2
20HSD-19	63.05	1.32	4.96	0.18772	0.00472	1.24864	0.03203	0.04774	0.00105	0.17	2722.3	41.4	822.8	14.5	300.6	6.5	249.6	5.8
20HSD-20	6.05	1.50	2.81	0.65840	0.01386	12.81584	0.29891	0.14491	0.00413	0.74	4642.5	30.4	2666.2	22.0	872.4	23.2	241.0	27.2
20HSD-21	33.04	0.79	3.10	0.25930	0.00650	1.88656	0.05835	0.05227	0.00104	0.26	3242.5	39.5	1076.4	20.5	328.4	6.4	243.6	5.9
20HSD-22	43.38	0.97	4.20	0.24387	0.00419	1.79612	0.03805	0.05290	0.00096	0.24	3145.4	27.3	1044.0	13.8	332.3	5.9	252.9	5.2
20HSD-23	50.73	4.21	4.30	0.22199	0.00368	1.53751	0.03320	0.04973	0.00087	0.22	2995.2	26.6	945.5	13.3	312.9	5.4	246.5	4.8
20HSD-24	51.08	0.81	4.43	0.21896	0.00713	1.50969	0.04952	0.04956	0.00104	0.21	2973.1	52.5	934.3	20.0	311.8	6.4	247.0	6.1
20HSD-25	22.29	1.90	3.01	0.32715	0.01017	3.05334	0.11552	0.06828	0.00179	0.34	3603.8	47.7	1421.1	28.9	425.8	10.8	284.0	10.1
20HSD-26	6.51	8.03	2.96	0.64805	0.01239	12.47656	0.28258	0.14027	0.00281	0.74	4619.6	27.6	2641.0	21.3	846.2	15.9	229.4	16.6
20HSD-27	16.73	0.59	2.42	0.39693	0.01000	3.78098	0.12830	0.06829	0.00152	0.44	3897.5	37.9	1588.7	27.2	425.8	9.2	242.9	7.9
20HSD-28	45.25	0.37	4.01	0.22525	0.00452	1.56807	0.03313	0.05016	0.00091	0.22	3018.6	32.2	957.7	13.1	315.5	5.6	247.7	5.0
20HSD-29	16.37	1.89	2.94	0.42165	0.00766	4.15584	0.07173	0.07254	0.00126	0.45	3988.1	27.2	1665.4	14.1	451.5	7.5	250.0	7.0
20HSD-30	39.75	0.17	3.68	0.24188	0.00682	1.70413	0.04781	0.05103	0.00111	0.24	3132.4	44.8	1010.1	18.0	320.8	6.8	245.7	6.1
HDG																		
20HLD-01	6.24	7.62	1.66	0.51742	0.01395	6.07152	0.16421	0.08826	0.00206	0.56	4291.6	39.6	1986.2	23.6	545.2	12.2	246.1	11.5
20HLD-02	5.56	8.89	1.47	0.50774	0.01579	5.99599	0.15551	0.08885	0.00189	0.55	4263.8	45.8	1975.3	22.6	548.7	11.2	254.2	12.3
20HLD-03	4.61	3.76	1.36	0.54213	0.01473	6.93098	0.17933	0.09689	0.00218	0.58	4360.1	39.8	2102.6	23.0	596.2	12.8	254.8	13.8
20HLD-04	21.33	33.97	2.57	0.26634	0.01138	1.99127	0.10029	0.05360	0.00137	0.27	3284.6	67.1	1112.6	34.0	336.6	8.4	246.5	7.8
20HLD-05	13.48	12.41	1.90	0.33304	0.01053	2.74746	0.08286	0.06197	0.00137	0.34	3631.1	48.4	1341.4	22.5	387.6	8.3	259.4	7.7
20HLD-06	6.37	5.72	1.51	0.48772	0.01556	5.66820	0.19756	0.08604	0.00200	0.53	4204.5	47.1	1926.5	30.1	532.0	11.9	254.1	12.1
20HLD-08	4.66	5.17	1.37	0.55368	0.02078	7.27099	0.28841	0.09973	0.00316	0.60	4390.9	54.9	2145.3	35.4	612.8	18.5	254.5	17.1

**Table 2.** Cont.

Spot No.	Isotope Ratios										$f_{206}$ %	Ages (Ma)						
	U ppm	Th ppm	Pb ppm	$^{207}\text{Pb}/^{206}\text{Pb}$	$\pm\sigma$	$^{207}\text{Pb}/^{235}\text{U}$	$\pm\sigma$	$^{206}\text{Pb}/^{238}\text{U}$	$\pm\sigma$	$^{207}\text{Pb}/^{206}\text{Pb}$	$\pm\sigma$	$^{207}\text{Pb}/^{235}\text{U}$	$\pm\sigma$	$^{206}\text{Pb}/^{238}\text{U}$	$\pm\sigma$	$^{207}\text{Pb-corr.}$	$\pm\sigma$	
20HLD-09	10.04	5.58	1.63	0.38769	0.00989	3.45665	0.08461	0.06683	0.00135	0.40	3862.0	38.5	1517.4	19.3	417.0	8.2	251.6	7.5
20HLD-10	2.11	0.04	1.11	0.67887	0.01892	13.91494	0.34994	0.15774	0.00390	0.73	4686.6	40.1	2743.9	23.8	944.2	21.7	264.1	23.3
20HLD-11	4.34	4.86	1.34	0.57215	0.02133	7.36013	0.21720	0.09993	0.00258	0.60	4438.8	54.4	2156.1	26.4	614.0	15.1	250.7	17.2
20HLD-12	3.46	0.04	1.12	0.60007	0.02092	8.19995	0.20584	0.10658	0.00227	0.63	4508.2	50.6	2253.3	22.7	652.8	13.2	247.4	15.4
20HLD-13	5.15	2.83	1.28	0.48278	0.01360	5.51520	0.13011	0.08711	0.00184	0.51	4189.5	41.6	1903.0	20.3	538.4	10.9	269.9	10.8
20HLD-14	4.86	4.49	1.43	0.54925	0.01415	7.03633	0.16924	0.09615	0.00201	0.60	4379.2	37.7	2116.0	21.4	591.8	11.8	243.9	11.7
20HLD-15	7.48	8.76	1.61	0.45719	0.01501	4.87104	0.14532	0.07938	0.00167	0.49	4108.8	48.8	1797.3	25.1	492.4	10.0	255.0	10.3
20HLD-16	5.47	6.80	1.32	0.50381	0.01358	5.43992	0.13158	0.08183	0.00183	0.54	4252.4	39.7	1891.2	20.7	507.0	10.9	239.1	10.2
20HLD-17	5.91	6.80	1.66	0.53878	0.01436	6.64138	0.15096	0.09324	0.00203	0.58	4351.0	39.0	2064.9	20.1	574.7	12.0	247.0	11.8
20HLD-18	2.36	0.00	1.13	0.67037	0.01918	12.44707	0.28854	0.14276	0.00347	0.73	4668.5	41.2	2638.7	21.8	860.2	19.6	247.6	22.4
20HLD-19	4.64	2.89	1.40	0.56953	0.01963	7.99498	0.35574	0.10443	0.00354	0.63	4432.1	50.3	2230.5	40.2	640.3	20.7	244.7	18.8
20HLD-20	7.45	6.86	1.49	0.45472	0.01525	4.55321	0.13386	0.07522	0.00171	0.48	4100.7	49.8	1740.7	24.5	467.5	10.3	245.3	10.8
20HLD-21	6.92	7.09	1.44	0.46703	0.01451	5.00009	0.15405	0.08070	0.00194	0.50	4140.4	46.1	1819.3	26.1	500.3	11.6	256.5	11.1
20HLD-22	6.90	8.53	1.46	0.46944	0.01338	4.88610	0.11578	0.07856	0.00172	0.50	4148.0	42.2	1799.9	20.0	487.5	10.3	248.7	9.8
20HLD-23	3.57	3.02	1.40	0.63136	0.02125	10.35219	0.30480	0.12453	0.00353	0.69	4581.9	48.7	2466.8	27.3	756.6	20.2	244.9	21.8
20HLD-24	3.57	1.59	1.38	0.61703	0.01903	9.92926	0.26938	0.12353	0.00348	0.66	4548.6	44.7	2428.2	25.0	750.9	20.0	262.2	20.7
20HLD-25	6.50	9.61	1.52	0.48807	0.01207	5.36874	0.15586	0.08218	0.00199	0.53	4205.6	36.5	1879.9	24.8	509.1	11.8	245.4	10.2
20HLD-26	8.22	7.66	1.61	0.45615	0.01078	4.67844	0.11100	0.07691	0.00169	0.49	4105.4	35.1	1763.4	19.8	477.7	10.1	249.5	9.2
20HLD-27	4.96	9.13	1.47	0.58514	0.02110	7.59007	0.26337	0.09685	0.00252	0.65	4471.5	52.5	2183.7	31.1	595.9	14.8	217.2	17.5
20HLD-28	10.32	6.46	1.50	0.37701	0.01262	3.08144	0.08957	0.06139	0.00145	0.39	3819.8	50.6	1428.1	22.3	384.1	8.8	236.6	8.0
20HLD-29	11.11	10.13	1.75	0.38963	0.00951	3.38127	0.06942	0.06488	0.00126	0.41	3869.5	36.8	1500.1	16.1	405.2	7.6	242.9	7.1
20HLD-30	8.13	6.44	1.54	0.46592	0.01316	4.41615	0.09772	0.07218	0.00156	0.49	4136.8	41.9	1715.4	18.3	449.3	9.4	232.9	9.2

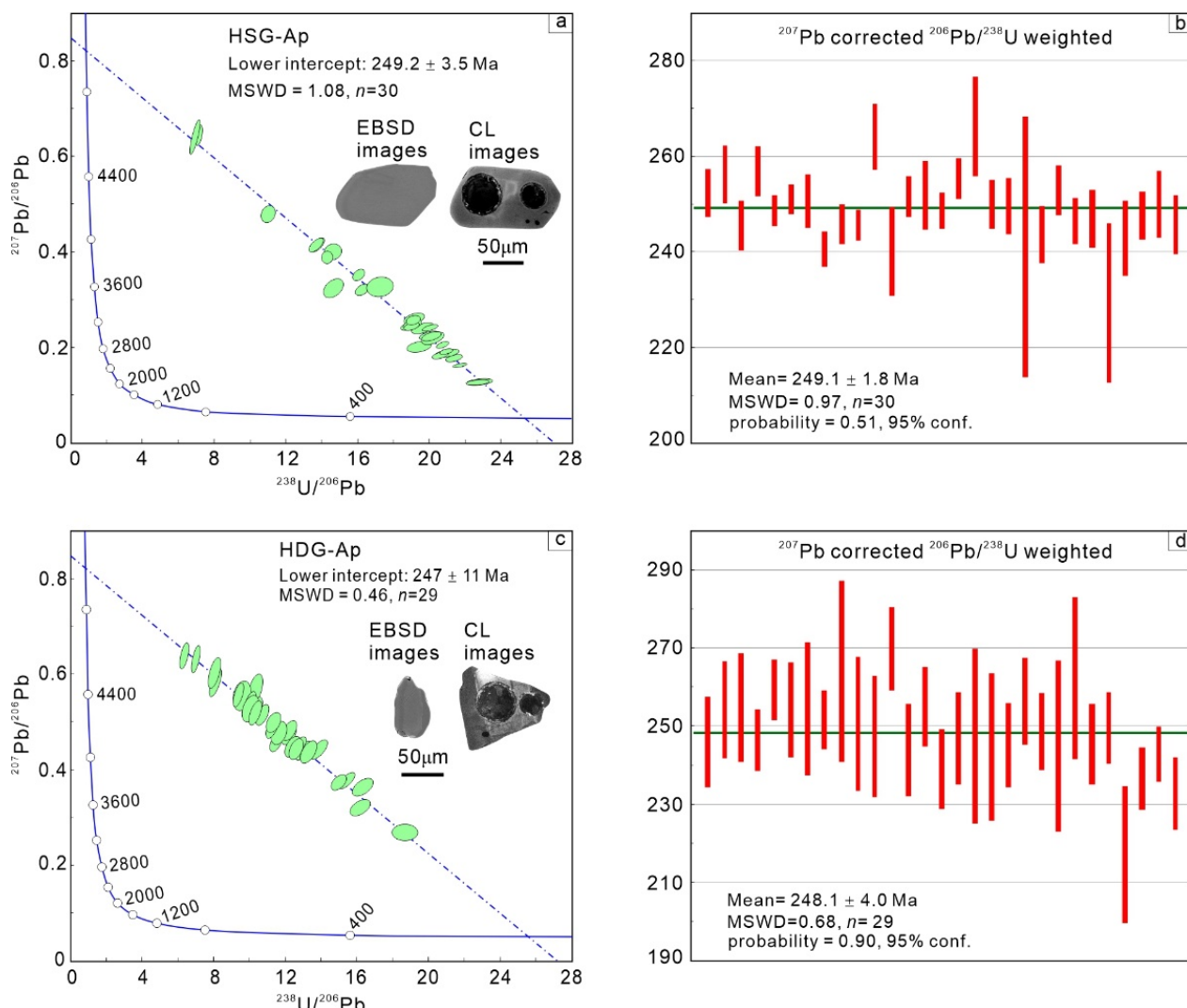


**Figure 5.** (a) U-Pb concordia diagram of the apatite from the HSG. (b) Weighted mean  $^{206}\text{Pb}/^{238}\text{U}$  age of the apatite from the HSG. (c) U-Pb concordia diagram of the apatite from the HDG. (d) Weighted mean  $^{206}\text{Pb}/^{238}\text{U}$  age of the apatite from the HDG.

#### 5.4. Zircon Hf Isotope

In situ zircon Hf isotopic analyses of HSG and HDG samples are presented in Table 6 and plotted in Figure 6. The initial  $^{176}\text{Hf}/^{177}\text{Hf}$  ratios of HSG ranged from 0.282972 to 0.2830656 (mean = 0.283016, n = 25), with calculated  $\epsilon_{\text{Hf}}(t)$  values ranging from 12.2 to 15.2. The two-stage Hf model ages ( $T_{\text{DM2}}$ ) range from 279.0 to 479.4 Ma, with an average of 381 Ma. The  $^{176}\text{Hf}/^{177}\text{Hf}$  ratios of HDG samples range from 0.282875 to 0.282920 (mean = 0.282903, n = 10), with calculated  $\epsilon_{\text{Hf}}(t)$  values ranging from 10.5 to 12.2 (mean = 11.6, n = 10). The two-stage Hf model ages ( $T_{\text{DM2}}$ ) range from 552 to 655 Ma, with an average of 589.9 Ma.

**Table 3.** Trace element compositions ( $10^{-6}$ ) of zircon grains from the HSG and HDG of the KDSZ.

Spot No.	La	Ce	Pr	Nd	Sm	Eu	Gd	Tb	Dy	Ho	Er	Tm	Yb	Lu	P	Sc	Ti	Y	Nb	Hf	Ta
HSG																					
20HSD-01	0.07	3.72	0.05	0.76	1.54	0.52	9.66	3.21	40.26	15.02	69.98	14.74	160.27	29.80	248.21	356.00	2.34	484.74	1.16	10973.90	0.22
20HSD-02	0.00	3.71	0.03	0.70	2.36	0.37	19.20	7.18	96.24	37.05	183.75	40.27	447.70	84.24	377.06	464.84	0.88	1152.38	3.13	11538.87	1.06
20HSD-03	0.00	3.18	0.04	0.87	2.80	0.62	16.55	5.36	64.28	22.93	103.26	20.75	218.22	38.79	288.60	385.22	6.13	759.27	1.31	10658.63	0.25
20HSD-04	0.00	2.47	0.03	0.78	1.99	0.36	13.60	4.90	59.21	20.90	95.54	19.67	204.33	36.85	244.23	427.48	1.47	690.11	1.50	11389.03	0.43
20HSD-05	0.00	11.63	0.03	0.80	2.96	1.08	20.41	7.75	105.45	42.19	202.12	42.52	453.19	83.88	449.82	546.32	3.31	1264.16	1.64	10762.89	0.47
20HSD-07	0.00	8.10	0.05	0.86	2.56	1.50	17.68	6.71	86.83	34.42	167.50	36.14	400.66	76.73	589.50	404.94	9.82	1033.26	0.96	8432.80	0.18
20HSD-08	0.00	8.42	0.05	1.14	3.12	1.25	23.00	7.55	91.23	31.63	143.33	28.29	297.61	53.71	302.03	385.79	4.18	994.34	1.89	10747.96	0.37
20HSD-09	0.01	6.50	0.06	1.15	3.19	1.11	20.82	7.17	92.11	34.64	160.02	32.73	348.21	63.26	374.46	445.13	6.82	1110.94	2.21	10720.18	0.33
20HSD-10	0.12	11.51	0.11	1.30	2.97	0.84	18.22	6.73	90.68	35.95	174.72	36.14	394.16	71.18	415.77	538.11	6.61	1080.11	1.52	11576.79	0.43
20HSD-11	0.00	14.64	0.03	1.10	3.30	1.33	24.23	8.89	114.28	43.93	203.73	41.11	433.65	77.04	428.57	532.14	3.82	1287.99	1.30	10359.39	0.31
20HSD-12	0.00	4.05	0.02	0.61	1.44	0.67	9.96	3.33	43.06	16.56	79.09	16.83	188.45	36.14	434.83	340.38	4.57	512.66	0.87	9888.66	0.20
20HSD-13	0.00	9.51	0.06	1.33	3.66	1.82	23.82	8.60	112.17	43.40	203.66	40.67	430.83	77.67	715.47	447.83	9.49	1325.98	1.57	8701.18	0.27
20HSD-14	0.02	3.40	0.10	1.73	5.03	0.79	28.91	9.59	107.78	36.24	152.80	29.93	306.50	52.35	519.24	477.67	5.13	1144.47	1.51	11721.04	0.32
20HSD-15	0.00	11.09	0.02	0.89	2.84	0.94	18.21	6.61	84.90	32.32	153.96	31.74	335.49	61.59	564.58	466.36	6.37	976.47	1.13	9319.26	0.29
20HSD-16	0.00	5.85	0.04	0.87	2.40	1.59	19.40	7.02	93.99	37.78	188.11	39.57	442.50	85.40	365.88	460.32	9.13	1144.56	1.11	8369.95	0.15
20HSD-17	0.00	3.75	0.01	0.30	1.15	0.42	8.25	3.19	41.05	15.77	77.43	15.82	176.99	32.42	305.04	340.13	2.13	472.73	0.90	12139.13	0.26
20HSD-18	0.05	11.02	0.10	1.25	2.64	0.95	17.06	6.01	78.15	30.80	145.45	29.93	323.84	58.65	353.66	485.07	3.58	912.06	1.13	10517.98	0.26
20HSD-19	0.00	11.35	0.03	0.99	3.42	1.45	23.43	8.23	107.09	40.52	191.07	39.13	420.71	76.26	383.17	471.17	5.16	1218.32	1.46	9967.16	0.35
20HSD-20	0.00	15.02	0.05	1.02	3.74	1.68	32.67	11.63	145.19	53.12	243.80	48.71	508.27	88.41	428.73	513.78	5.90	1574.45	1.39	10792.45	0.34
20HSD-22	0.01	3.20	0.04	0.88	2.92	0.44	15.55	5.53	66.12	24.06	110.46	22.83	245.52	44.43	315.11	416.37	2.16	765.20	1.66	11310.36	0.41
20HSD-23	4.05	23.83	1.93	10.33	4.73	1.19	20.15	7.19	90.00	35.22	165.91	33.61	358.07	64.46	2561.04	470.78	5.64	1037.54	1.20	9446.60	0.25
20HSD-24	0.00	10.81	0.08	1.41	3.72	1.83	24.21	9.24	121.15	47.57	226.13	46.34	502.00	93.34	532.47	505.17	10.25	1451.57	1.78	9406.52	0.33
20HSD-25	0.08	10.55	0.14	1.44	2.55	1.57	19.45	7.65	101.89	41.22	200.90	42.83	470.40	84.35	495.38	522.69	4.25	1224.79	1.43	11529.37	0.52
20HSD-26	0.00	10.00	0.06	1.10	3.12	2.04	28.64	10.19	127.06	48.48	230.65	47.99	512.94	94.91	432.54	408.99	9.46	1451.60	1.06	8578.40	0.19
20HSD-27	0.00	4.72	0.01	0.29	1.14	0.32	10.19	4.15	56.31	23.29	117.24	25.71	293.87	55.40	332.57	348.34	0.59	692.44	2.08	11461.53	0.61
20HSD-28	0.00	2.79	0.02	0.25	0.86	0.24	5.96	2.35	29.93	11.79	58.51	12.88	151.87	29.38	368.05	302.89	4.06	362.22	1.02	10289.09	0.30
20HSD-29	0.00	12.80	0.05	0.98	3.18	1.23	22.29	7.75	99.41	37.81	178.47	36.34	384.62	70.03	363.33	500.29	4.22	1126.31	1.37	10089.38	0.32
20HSD-30	0.00	2.49	0.03	0.76	2.53	0.40	14.72	5.26	61.05	20.66	84.11	16.35	167.91	28.14	233.90	418.81	3.27	654.28	1.56	11449.89	0.38

**Table 3.** *Cont.*

Spot No.	La	Ce	Pr	Nd	Sm	Eu	Gd	Tb	Dy	Ho	Er	Tm	Yb	Lu	P	Sc	Ti	Y	Nb	Hf	Ta
HDG																					
20HLD-01	0.02	0.53	0.01	0.15	0.28	0.08	1.19	0.41	4.31	1.77	7.55	1.65	15.70	3.23	339.02	342.69	8.42	1149.03	1.63	9850.39	0.51
20HLD-03	0.05	0.57	0.02	0.18	0.26	0.10	0.91	0.33	3.77	1.46	6.82	1.60	15.33	3.49	690.29	339.47	8.56	1228.32	1.87	9616.76	0.55
20HLD-05	0.04	0.45	0.03	0.18	0.25	0.08	0.85	0.24	2.42	0.98	4.70	1.23	11.29	2.59	544.54	356.69	5.65	1430.99	2.00	9415.22	0.59
20HLD-06	0.06	0.48	0.04	0.30	0.30	0.10	0.76	0.22	2.35	0.89	4.34	1.06	11.41	2.22	972.75	341.19	6.89	963.37	1.72	9628.53	0.56
20HLD-07	0.39	3.52	0.19	1.07	0.49	0.11	0.79	0.21	2.12	0.86	4.31	1.02	11.40	2.32	2482.14	341.06	12.10	1068.81	1.48	9662.93	0.51
20HLD-09	0.01	0.77	0.02	0.19	0.25	0.11	0.89	0.29	3.55	1.62	8.05	2.12	21.22	4.82	614.68	416.71	9.14	2142.45	2.56	8420.94	0.67
20HLD-10	0.15	0.74	0.06	0.31	0.23	0.07	0.80	0.24	2.92	1.25	5.91	1.44	15.00	3.14	433.19	348.28	10.07	941.37	1.46	9777.20	0.54
20HLD-11	0.65	8.61	0.20	1.20	1.26	0.40	7.16	2.52	34.46	14.92	73.63	17.82	193.95	40.24	525.74	228.10	58.06	466.20	1.15	8996.50	0.34
20HLD-12	0.06	12.04	0.05	0.79	1.60	0.68	12.08	4.24	57.49	24.00	121.04	28.20	304.02	61.61	65.43	269.01	12.10	765.91	1.05	8912.85	0.36
20HLD-13	0.03	23.42	0.08	1.60	3.68	1.39	24.94	9.63	130.60	56.26	281.76	65.49	710.89	143.01	31.45	316.20	9.14	1774.49	2.80	8699.90	0.84
20HLD-14	0.58	20.23	0.16	1.68	2.09	0.51	12.09	4.88	70.71	30.66	154.47	36.76	397.45	79.76	392.05	256.33	17.62	978.18	4.46	10551.10	1.39
20HLD-15	1.28	49.97	1.48	8.95	7.47	1.93	29.09	9.67	120.34	47.31	222.05	50.14	529.83	104.95	1083.61	258.59	8.42	1444.92	2.25	9951.31	0.83
20HLD-16	0.00	10.37	0.03	0.99	2.10	0.91	13.77	5.13	65.72	27.51	134.63	30.59	320.05	65.95	0.00	268.51	8.56	860.92	0.93	8703.77	0.44
20HLD-17	0.64	24.26	0.34	2.40	4.87	0.95	16.07	5.76	79.54	33.54	173.73	41.59	461.91	95.44	4357.60	286.58	5.65	1078.18	3.13	9765.72	1.14
20HLD-18	0.82	27.04	0.64	4.65	4.22	1.26	20.13	6.84	92.60	38.98	197.39	45.55	493.90	100.54	305.64	279.97	6.89	1243.26	3.16	9670.60	1.02
20HLD-19	0.03	20.72	0.15	2.37	5.30	1.87	30.31	10.87	144.35	58.36	283.50	65.07	684.45	137.50	105.91	297.40	10.07	1835.63	2.00	8649.84	0.65
20HLD-20	0.71	12.71	0.36	2.34	1.90	0.79	13.11	4.66	62.65	27.00	136.48	32.20	355.37	72.72	764.27	262.24	13.69	869.06	1.91	8593.78	0.50

**Table 4.** Major element compositions ( $10^{-2}$ ) of apatite grains from the HSG and HDG of the KDSZ.

Spot No.	Al <sub>2</sub> O <sub>3</sub>	P <sub>2</sub> O <sub>5</sub>	Ce <sub>2</sub> O <sub>3</sub>	SiO <sub>2</sub>	K <sub>2</sub> O	CaO	PbO	SO <sub>3</sub>	La <sub>2</sub> O <sub>3</sub>	Na <sub>2</sub> O	MgO	MnO	Pr <sub>2</sub> O <sub>3</sub>	FeO	TiO <sub>2</sub>	F	Cl	Total	
HSG																			
20HSD-01	0.055	41.922	0.071	0.121	0.245	54.09	0.052	0	0	0.184	0.067	0.789	0	0.196	0.048	3.098	0.062	99.72	
20HSD-02	0.006	42.681	0.117	0.019	0.105	54.14	0	0.02	0	0	0.031	0.774	0	0.148	0.041	3.975	0.024	100.45	
20HSD-03	0.023	41.355	0.111	0.046	0.024	54.78	0.026	0.02	0.025	0	0	0.601	0.084	0.087	0	3.321	0.012	99.13	
20HSD-04	0	42.14	0.116	0.065	0.065	53.17	0	0	0.302	0.005	0.012	0.444	0.003	0.074	0.01	3.899	0.019	98.73	
20HSD-05	0.006	41.783	0.075	0.052	0.042	54.48	0.045	0	0.025	0.015	0.036	0.816	0.023	0.218	0	2.983	0.027	99.41	
20HSD-06	0.034	42.046	0.077	0.04	0.18	53.94	0	0.01	0.15	0.103	0.016	0.652	0	0.114	0.01	3.137	0.049	99.28	
20HSD-07	0.005	41.391	0	0.085	0.222	54.94	0.013	0.02	0	0.294	0	0.401	0.037	0.028	0.029	3.148	0.07	99.36	
20HSD-08	0	42.429	0.1	0.016	0.125	53.42	0	0.07	0.075	0.074	0.011	0.615	0	0.066	0	3.153	0.037	98.88	
20HSD-09	0.053	42.532	0.088	0.107	0.21	53.62	0.076	0.07	0.025	0.221	0	0.565	0	0.103	0	3.876	0.076	99.97	
20HSD-10	0.021	42.387	0.113	0.025	0.044	54.35	0	0.04	0.074	0.034	0	0.326	0.007	0.042	0.054	3.179	0.068	99.42	
20HSD-11	0.007	42.113	0.047	0.058	0.012	54.15	0.019	0.02	0.148	0	0	0.327	0	0.062	0.022	2.939	0.016	98.73	
20HSD-13	0.005	41.928	0.087	0.028	0.007	54.44	0	0.01	0	0	0.013	0.689	0	0.192	0.002	3.866	0.025	99.69	
20HSD-14	0.033	41.551	0.131	0.204	0.285	53.94	0	0.04	0.049	0.213	0.016	0.609	0	0.05	0.044	4.099	0.061	99.67	
20HSD-15	0.004	41.514	0.053	0.106	0.112	54.67	0	0.03	0	0.17	0.019	0.67	0.085	0.129	0	3.995	0.055	99.96	
20HSD-16	0	41.278	0.069	0.025	0.058	53.91	0	0	0.053	0.016	0.776	0.101	0.16	0.018	4.029	0.027	98.87		
20HSD-17	0.001	41.817	0.084	0.137	0.068	54.51	0.006	0.01	0.146	0.067	0	0.596	0.023	0.115	0.006	2.895	0.031	99.31	
20HSD-18	0.021	42.313	0.059	0.056	0.149	54.86	0.012	0.02	0	0.016	0	0.333	0	0.045	0.008	3.27	0.025	99.80	
20HSD-19	0.005	41.826	0.142	0.037	0.236	53.49	0	0.02	0	0.228	0.039	0.438	0	0.043	0.024	3.42	0.067	98.55	
20HSD-20	0.003	42.444	0.143	0.036	0.024	54.23	0	0.05	0.194	0	0	0.642	0	0.169	0.038	3.084	0.033	99.78	
HDG																			
20HLD-01	0	42.227	0.039	0.001	0.038	55.34	0	0.03	0	0	0	0.092	0.026	0	0	2.572	0.029	99.30	
20HLD-02	0	42.528	0.056	0.033	0	54.23	0	0.03	0.145	0	0	0.08	0	0.024	0	3.279	0.025	99.08	
20HLD-03	0.033	42.229	0.05	0.07	0.04	54.16	0.055	0.03	0	0	0	0.093	0	0.013	0.02	4.147	0.029	99.24	
20HLD-04	0.014	42.199	0	0.065	0.028	55.83	0	0.05	0	0	0	0.021	0.065	0	0.029	0	2.594	0.022	99.84
20HLD-05	0.006	42.824	0.025	0.091	0.002	53.9	0.012	0.05	0	0	0	0.034	0.083	0	0.018	0	2.95	0.033	98.78
20HLD-06	0	41.825	0.032	0.031	0.008	55.18	0	0.05	0	0	0	0.049	0.077	0.028	0	2.741	0.026	98.88	
20HLD-07	0.053	42.098	0.067	0.264	0.1	54.73	0	0.07	0.048	0	0.024	0.044	0	0.001	0	2.951	0.03	99.26	
20HLD-08	0.018	42.87	0.016	0.055	0.004	55.3	0	0.02	0	0	0	0.014	0.149	0	0	1.892	0.012	99.55	
20HLD-09	0.014	42.96	0	0.059	0.039	54.82	0.012	0.01	0.024	0	0	0.141	0.013	0.02	0.01	3.066	0.058	99.95	
20HLD-10	0	42.378	0.006	0.081	0.052	54.79	0	0.03	0	0	0	0.067	0	0.048	0.012	2.773	0.017	99.11	
20HLD-11	0.047	42.646	0.016	0.096	0.013	54.85	0	0.06	0.072	0	0.012	0.063	0.093	0.014	0	2.786	0.024	99.60	
20HLD-12	0.001	42.5	0.005	0.077	0.002	54.05	0.104	0.02	0.167	0	0	0.078	0	0.029	0.027	2.542	0.022	98.55	
20HLD-13	0	42.505	0.039	0.048	0	54.32	0.037	0.03	0	0	0.023	0.101	0	0	0	2.737	0.01	98.77	
20HLD-14	0	42.747	0	0.061	0.003	54.6	0	0.04	0	0	0	0.069	0.01	0.008	0.036	2.611	0.009	99.12	
20HLD-16	0	42.427	0.014	0.045	0.016	54.94	0	0.05	0.144	0	0.012	0.128	0.026	0.031	0	3.326	0.019	99.85	
20HLD-17	0.021	42.326	0.029	0.101	0.011	55.14	0	0.01	0.072	0	0	0.11	0	0.027	0	2.648	0.035	99.48	
20HLD-18	0.008	41.409	0.044	0.041	0.005	54.57	0.074	0.07	0	0	0.002	0.108	0.061	0.019	0.004	3.621	0.041	98.57	
20HLD-19	0.025	42.849	0	0.073	0.001	54.29	0.031	0.06	0	0	0	0.071	0	0.018	0	2.817	0.019	99.11	
20HLD-20	0.011	42.535	0.01	0.035	0.004	54.35	0	0.04	0	0	0	0.109	0.051	0.005	0	2.556	0.004	98.67	

**Table 5.** Trace element compositions ( $10^{-6}$ ) of apatite grains from the HSG and HDG of the KDSZ.

Spot No.	P	Mn	Sr	Y	La	Ce	Pr	Nd	Sm	Eu	Gd	Tb	Dy	Ho	Er	Tm	Yb	Lu	$\Sigma$ REE	LREE	HREE	$\delta$ Eu	$\delta$ Ce
HSG																							
20HSD-01	252000	7960	138	1730	127	589	103	552	326	10	376	70.5	372	58.5	143	20.5	137	16.8	1866.2	1012.0	854.2	0.21	1.10
20HSD-02	228000	6980	380	1250	234	842	141	703	254	17.4	286	43.5	255	42.3	108	14.2	86.1	10.7	3037.20	2191.4	845.8	0.20	1.14
20HSD-03	222000	7330	172	1760	148	653	127	693	330	10.8	398	66	384	65.8	165	20.4	122	15.5	3198.50	1961.8	1236.7	0.09	1.17
20HSD-04	231000	5690	181	1580	125	527	97.9	530	298	12.1	377	64.6	365	56.3	138	19.2	124	15.3	2749.40	1590.0	1159.4	0.11	1.17
20HSD-05	242000	6410	170	2490	201	900	171	934	480	16.9	573	95.7	553	89.6	229	32.6	218	29	4522.80	2702.9	1819.9	0.10	1.19
20HSD-06	204000	6500	150	1700	134	528	98.3	543	307	10.1	387	69.6	397	60.2	149	20.6	131	16.5	2851.30	1620.4	1230.9	0.09	1.13
20HSD-07	238000	5920	157	1590	126	535	97.5	552	302	11.6	391	68.5	379	58	146	19.9	129	15.2	2830.7	1624.1	1206.6	0.10	1.18
20HSD-08	234000	3210	160	1540	104	475	91.2	526	315	9.87	396	69.8	375	57.4	138	18.5	117	14.2	2706.97	1521.1	1185.9	0.09	1.20
20HSD-09	218000	6490	153	1670	133	567	104	554	312	13.5	378	66.4	373	59.2	149	21.1	136	16.7	2882.90	1683.5	1199.4	0.12	1.18
20HSD-10	213000	4940	155	1570	115	485	90.5	492	269	11.1	333	59.7	338	56	138	18.3	116	14.1	2535.7	1462.6	1073.1	0.11	1.17
20HSD-11	195000	5930	154	1980	147	627	113	627	379	15.4	463	82.6	460	69.1	170	23.5	153	19.6	3349.2	1908.4	1440.8	0.11	1.19
20HSD-12	239000	7540	177	1790	150	571	107	553	316	12.6	385	70.2	396	63.7	163	22.3	146	18.6	2974.4	1709.6	1264.8	0.11	1.11
20HSD-13	216000	6430	180	2210	182	803	152	843	415	17	478	83.4	476	76.5	196	26.4	174	21.5	3943.8	2412.0	1531.8	0.12	1.18
20HSD-14	221000	7850	163	1770	143	578	106	559	326	10.6	398	71.3	405	63.8	158	22.7	146	18.6	3006	1722.6	1283.4	0.09	1.15
20HSD-15	229000	6140	150	1750	139	555	108	583	344	11	435	76.3	426	64.8	162	22	146	18.1	3090.2	1740.0	1350.2	0.09	1.11
20HSD-16	239000	7570	212	2630	280	1080	207	1100	481	20.3	553	94.1	531	88.6	224	31	206	25.7	4921.7	3168.3	1753.4	0.12	1.10
20HSD-17	187000	5240	182	1610	122	497	95	527	294	9.87	378	66.8	376	57.2	140	19.8	127	15.4	2725.07	1544.9	1180.2	0.09	1.13
20HSD-18	220000	2570	154	1410	87.1	392	78.9	451	273	9.11	364	63.3	339	48.9	118	15.5	94.7	11.3	2345.81	1291.1	1054.7	0.09	1.16
20HSD-19	234000	7190	243	1500	165	648	121	640	267	13.1	305	49.3	290	50.5	131	16.3	94.2	11.6	2802	1854.1	947.9	0.14	1.12
HDG																							
20HLD-01	225000	775	182	1930	106	419	80.6	494	190	25.5	285	44.7	295	66	199	27.2	178	32.6	2442.60	1315.1	1127.5	0.34	1.11
20HLD-02	313000	732	138	792	5.79	24.5	5.49	37.9	25.8	9.75	60.5	12.7	106	27.8	91.4	13.4	83.6	15.4	520.03	109.2	410.8	0.75	1.07
20HLD-03	161000	651	166	3300	13.8	65.8	16.5	121	82.6	30	194	44.1	383	102	362	56	402	65.8	1938.60	329.7	1608.9	0.72	1.07
20HLD-04	223000	562	220	1400	7.91	40	10.3	81.3	55	25.9	117	22.1	171	44.8	155	23.6	162	33.5	949.41	220.4	729.0	0.99	1.09
20HLD-05	206000	771	149	1090	6.91	27.7	6.39	47.3	29.5	10.3	68.9	15.5	132	35.1	122	18.1	122	21.2	662.90	128.1	534.8	0.70	1.02
20HLD-06	212000	714	153	266	2.25	10.4	2.45	16.2	9.56	4.5	19.2	3.73	30.1	8.02	27.7	4	27.3	5.46	170.87	45.4	125.5	1.02	1.09
20HLD-07	216000	529	144	1010	11.9	43.3	9.97	66.2	33.2	21.2	70.8	14	112	31.5	116	17.4	130	26.8	704.27	185.8	518.5	1.34	0.97
20HLD-08	200000	851	176	709	21	74.3	13.5	84.3	35.5	8.31	66.1	13.5	104	25.2	77.5	10.5	66.9	12.1	612.71	236.9	375.8	0.52	1.08
20HLD-09	241000	757	176	621	5.65	16.3	4.79	32.1	16.7	9.44	38.2	7.53	65.8	18.2	68.1	10.2	73.3	14.1	380.41	85.0	295.4	1.14	0.77
20HLD-10	249000	769	154	2040	12.2	59.5	14.2	112	65.6	24.1	147	29.5	237	64	231	35.2	255	44.6	1330.9	287.6	1043.3	0.75	1.11
20HLD-11	202000	664	178	1240	43.9	182	36.1	236	100	16.6	165	27.4	185	42.8	134	18	113	20.7	1320.5	614.6	705.9	0.40	1.12
20HLD-12	198000	609	177	1350	13.1	46.9	12.5	90	57.4	27.4	115	21.3	161	42.3	145	21.7	153	31.1	937.7	247.3	690.4	1.03	0.90
20HLD-13	210000	727	173	1750	24	77	19.5	137	71.4	22	145	28.7	223	57.2	193	28.1	190	34.3	1250.2	350.9	899.3	0.66	0.87
20HLD-14	210000	574	189	668	7.05	38.1	7.61	56.8	33.4	15	68.7	12.1	91.6	23.4	80.4	11.4	78.6	16.4	540.56	158.0	382.6	0.96	1.28
20HLD-15	220000	673	251	803	37.2	163	35.3	224	86.9	9.61	114	19	123	26.2	83.5	10.8	71.7	12.8	171.81	59.8	112.0	0.85	0.55
20HLD-16	228000	767	146	2010	12.8	51.5	11.7	86	51.7	18.7	125	28.2	248	65.2	238	35	234	41.1	1017.01	556.0	461.0	0.30	1.10
20HLD-17	220000	493	164	448	5.89	25.6	5.67	39.6	18.7	11.4	37.8	6.81	52.3	14.1	50.5	7.72	53.3	11.3	1246.9	232.4	1014.5	0.71	1.03
20HLD-18	205000	685	148	321	1.78	6.74	1.58	12.2	7.87	4.7	17.9	3.78	31.9	9.25	34.5	5.17	36.1	7.15	340.69	106.9	233.8	1.31	1.09
20HLD-19	185000	854	230	1420	78.2	317	63.3	388	153	12.5	219	35.3	238	51.3	155	19.2	118	18.4	180.62	34.9	145.8	1.21	0.99

**Table 6.** Hf isotope composition of zircon grains from HSG and HDG of the KDSZ.

Spot No.	T(Ma)	$^{176}\text{Yb}/^{177}\text{Hf}$	1σ	$^{176}\text{Lu}/^{177}\text{Hf}$	1σ	$^{176}\text{Hf}/^{177}\text{Hf}$	1σ	$\varepsilon\text{Hf}(0)$	$\varepsilon\text{Hf(t)}$	$T_{\text{DM}} \text{ (Ma)}$	$T_{2\text{DM}} \text{ (Ma)}$	$f_{\text{Lu/Hf}}$
HSG												
20HSD-01	254.0	0.011629	0.000127	0.000454	0.000004	0.283014	0.000009	8.1	13.7	333	381	-0.99
20HSD-02	258.1	0.027567	0.000122	0.001080	0.000002	0.282972	0.000008	6.6	12.2	397	479	-0.97
20HSD-03	251.9	0.013551	0.000615	0.000501	0.000021	0.283002	0.000009	7.7	13.2	350	410	-0.99
20HSD-04	251.4	0.012154	0.000229	0.000449	0.000009	0.282992	0.000010	7.3	12.8	363	433	-0.99
20HSD-05	254.2	0.029700	0.000778	0.001119	0.000026	0.283022	0.000008	8.4	13.8	327	370	-0.97
20HSD-06	267.1	0.026272	0.000172	0.001006	0.000008	0.283038	0.000009	9.0	14.7	303	324	-0.97
20HSD-07	258.9	0.028854	0.000339	0.001177	0.000010	0.283021	0.000010	8.3	13.9	328	369	-0.96
20HSD-08	248.4	0.030252	0.000447	0.001141	0.000013	0.282981	0.000009	6.9	12.3	385	465	-0.97
20HSD-09	257.7	0.026652	0.000279	0.000979	0.000010	0.282977	0.000009	6.8	12.3	390	469	-0.97
20HSD-10	254.0	0.027490	0.000266	0.001075	0.000009	0.283005	0.000008	7.8	13.2	351	408	-0.97
20HSD-11	259.8	0.028210	0.000315	0.001056	0.000011	0.283046	0.000010	9.2	14.8	292	310	-0.97
20HSD-12	260.6	0.027056	0.000271	0.001031	0.000009	0.283003	0.000008	7.7	13.3	352	407	-0.97
20HSD-13	259.0	0.041531	0.000300	0.001582	0.000011	0.283015	0.000009	8.1	13.6	341	388	-0.95
20HSD-14	260.6	0.027278	0.000880	0.001008	0.000032	0.282975	0.000010	6.7	12.3	392	471	-0.97
20HSD-16	259.3	0.039020	0.000233	0.001573	0.000006	0.283057	0.000011	9.6	15.1	279	291	-0.95
20HSD-18	262.5	0.046152	0.000545	0.001677	0.000018	0.283019	0.000008	8.3	13.8	337	379	-0.95
20HSD-19	254.6	0.030896	0.000167	0.001181	0.000006	0.283042	0.000009	9.1	14.5	299	326	-0.96
20HSD-20	258.9	0.032997	0.000223	0.001272	0.000007	0.283033	0.000011	8.8	14.3	312	343	-0.96
20HSD-21	261.5	0.028172	0.000123	0.001082	0.000004	0.283042	0.000009	9.1	14.7	298	320	-0.97
20HSD-23	259.2	0.030054	0.000260	0.001134	0.000012	0.283032	0.000009	8.7	14.3	312	343	-0.97
20HSD-24	255.7	0.041629	0.000365	0.001624	0.000016	0.283020	0.000009	8.3	13.7	334	378	-0.95
20HSD-25	249.0	0.038974	0.001030	0.001439	0.000037	0.283042	0.000010	9.1	14.4	301	331	-0.96
20HSD-26	250.1	0.044217	0.000331	0.001711	0.000011	0.283066	0.000009	9.9	15.2	269	279	-0.95
20HSD-28	256.8	0.014469	0.000344	0.000586	0.000011	0.283000	0.000011	7.6	13.2	353	412	-0.98
20HSD-30	264.8	0.014413	0.000072	0.000536	0.000003	0.282986	0.000009	7.1	12.9	372	438	-0.98
HDG												
20HLD-03	347.3	0.034900	0.000841	0.001100	0.000023	0.282906	0.000010	4.3	11.8	492	578	-0.97
20HLD-05	337.6	0.040700	0.000178	0.001270	0.000008	0.282912	0.000010	4.5	11.9	486	567	-0.96
20HLD-07	342.1	0.046900	0.000571	0.001500	0.000013	0.282920	0.000010	4.8	12.2	477	552	-0.96
20HLD-08	345.2	0.062400	0.001070	0.001930	0.000035	0.282903	0.000010	4.2	11.5	508	597	-0.94
20HLD-09	341.7	0.053700	0.000424	0.001710	0.000017	0.282899	0.000008	4.0	11.4	510	603	-0.95
20HLD-10	352.1	0.041200	0.000133	0.001290	0.000006	0.282914	0.000009	4.6	12.0	483	562	-0.96
20HLD-12	351.5	0.047300	0.000500	0.001530	0.000016	0.282906	0.000010	4.3	11.7	498	584	-0.95
20HLD-16	349.4	0.051100	0.000173	0.001590	0.000007	0.282875	0.000009	3.2	10.5	543	655	-0.95
20HLD-17	351.2	0.068400	0.000303	0.002100	0.000008	0.282897	0.000009	4.0	11.2	518	612	-0.94
20HLD-18	344.3	0.040500	0.001620	0.001270	0.000047	0.282902	0.000009	4.1	11.6	500	589	-0.96

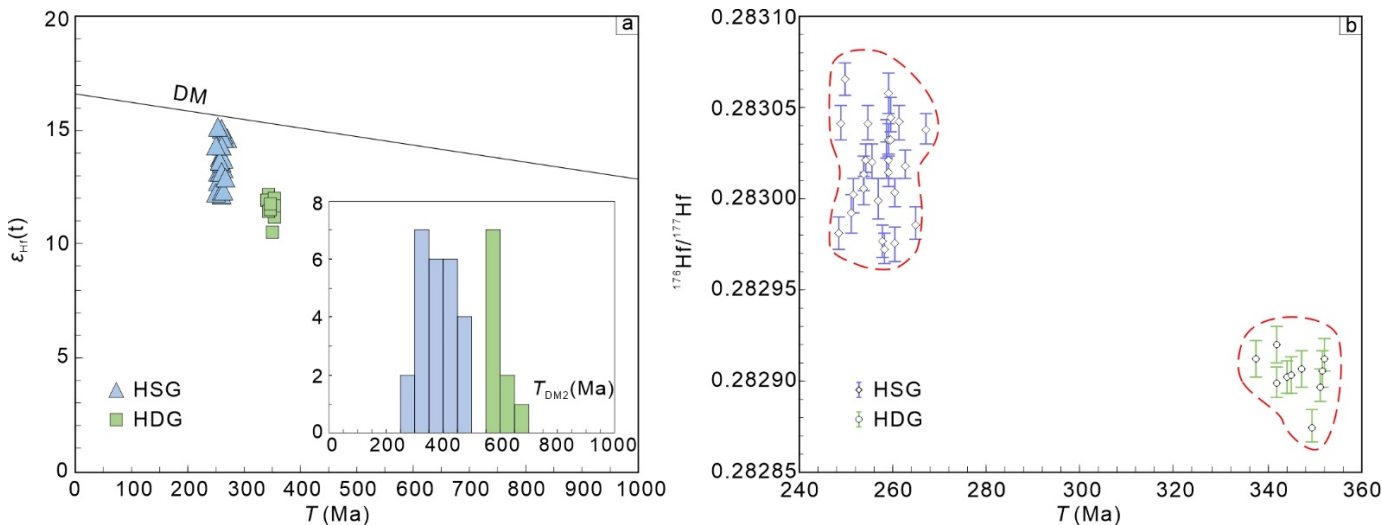


**Figure 6.** (a) In situ zircon Hf isotope diagram. (b) The initial  $^{176}\text{Hf}/^{177}\text{Hf}$  ratios from HSG and HDG.

### 5.5. Major and Trace Element Geochemistry of Granites

The whole-rock major and trace element data are presented in Table 7 and plotted in the “granite” compositional field in the TAS diagram (Figure 7a). Eight samples from HSG are characterized by high SiO<sub>2</sub> (71.90–72.99 wt.%), Al<sub>2</sub>O<sub>3</sub> (14.44–15.43 wt.%), and Na<sub>2</sub>O (4.42–5.29 wt.%) and low TiO<sub>2</sub> (0.16–0.21 wt.%), MgO (0.51–0.66 wt.%), and Fe<sub>2</sub>O<sub>3</sub><sup>T</sup> (1.42–1.90 wt.%) contents, indicating that HSG may belong to the calc-alkaline magmatic affinity (Figure 7b). All of the samples from HSG display relatively low A/CNK values (1.06–1.09) and are classified as peraluminous. Six samples from HDG are characterized by high SiO<sub>2</sub> (68.16–75.47 wt.%), Al<sub>2</sub>O<sub>3</sub> (12.58–16.92 wt.%), Na<sub>2</sub>O (3.44–5.16 wt.%), and K<sub>2</sub>O (2.55–4.24 wt.%) and low TiO<sub>2</sub> (0.28–0.37 wt.%), MgO (0.52–0.78 wt.%), and Fe<sub>2</sub>O<sub>3</sub><sup>T</sup> (1.54–2.08 wt.%) contents, exhibiting a calc-alkaline to high-K calc-alkaline magmatic affinity (Figure 7b). All of the samples from HSG display relatively low A/CNK values (1.01–1.08) and are classified as peraluminous.

The samples from HSG are characterized by low ΣREE (50.45–67.51 ppm), LREE enrichments and HREE depletions (LREE/HREE = 7.3–14.9), and weak negative Eu ( $\delta\text{Eu} = 0.65–1.10$ ) and weak negative Ce anomalies ( $\delta\text{Ce} = 0.96–0.97$ ) (Figure 7c). Moreover, they are also enriched in large-ion lithophile elements (LILEs; e.g., Rb, U, and K) and depleted in high-field-strength elements (HFSEs; e.g., Ta, Nb, P, and Ti; Figure 7d) compared to the primitive mantle. The samples from HDG are characterized by low ΣREE (64.90–91.40 ppm), LREE enrichment and HREE depletion (LREE/HREE = 5.2–8.0), and weak negative Eu ( $\delta\text{Eu} = 0.65–0.86$ ) and weak Ce anomalies ( $\delta\text{Ce} = 0.78–1.30$ ; Figure 7c). Furthermore, they are also enriched in LILEs (e.g., Rb, U, and K) and depleted in HFSEs (e.g., Ta, Nb, P, and Ti) compared to the primitive mantle (Figure 7d).

**Table 7.** Whole-rock geochemical compositions of the HSG and HDG of the KDSZ.

Sample No.	20HSD-Y1	20HSD-Y2	20HSD-Y3	20HSD-Y4	20HSD-Y5	20HSD-Y6	20HSD-Y7	20HSD-Y8	20HLD-Y1	20HLD-Y2	20HLD-Y3	20HLD-Y4	20HLD-Y5	20HLD-Y6
Name	HSG								HDG					
	Major elements (%)													
SiO <sub>2</sub>	72.69	72.97	71.9	72.55	72.64	72.54	72.52	72.99	73.63	73.14	68.16	75.47	73.81	73.23
TiO <sub>2</sub>	0.19	0.16	0.21	0.19	0.19	0.19	0.2	0.19	0.36	0.34	0.37	0.28	0.35	0.35
Al <sub>2</sub> O <sub>3</sub>	14.88	14.44	15.43	15.03	15.06	14.94	15.04	14.83	13.68	14.03	16.92	12.58	13.46	13.8
TFe <sub>2</sub> O <sub>3</sub>	1.74	1.42	1.9	1.74	1.72	1.67	1.71	1.71	1.88	2.04	2.05	1.54	1.81	2.08
FeO	1.39	1.16	1.36	1.31	1.36	1.31	1.31	1.36	0.78	0.8	0.59	0.39	0.9	0.8
Na <sub>2</sub> O + K <sub>2</sub> O	6.7	7.12	6.46	6.47	6.5	6.7	6.39	6.53	7.19	7.76	8.01	7.54	7.8	8.05
MnO	0.055	0.062	0.049	0.048	0.05	0.049	0.05	0.05	0.053	0.049	0.044	0.036	0.053	0.047
MgO	0.6	0.51	0.66	0.54	0.58	0.56	0.56	0.57	0.78	0.6	0.62	0.52	0.65	0.77
CaO	2.28	1.65	2.62	2.56	2.45	2.35	2.49	2.31	1.64	1.68	2.44	1.2	1.39	1.16
Na <sub>2</sub> O	4.42	5.29	4.66	4.58	4.66	4.63	4.69	4.61	4.64	4.72	5.16	3.44	4.22	3.81
K <sub>2</sub> O	2.28	1.83	1.8	1.89	1.84	2.07	1.7	1.92	2.55	3.04	2.85	4.1	3.58	4.24
P <sub>2</sub> O <sub>5</sub>	0.08	0.062	0.089	0.078	0.083	0.08	0.087	0.074	0.11	0.1	0.11	0.082	0.1	0.11
S	0.12	0.15	0.15	0.05	0.16	0.07	0.07	0.21	0.065	0.06	0.12	0.09	0.04	0.08
LOI	0.68	1.24	0.68	0.71	0.58	0.57	0.63	0.8	0.84	0.65	0.91	0.66	1	0.72
Total	99.96	99.72	100.10	99.92	99.96	99.67	99.70	100.21	100.18	100.40	99.71	99.96	100.41	100.35
	Trace elements (ppm)													
La	13.3	14	10.6	13.8	12.9	12.2	13.2	11.9	12.8	16.8	13.8	14	21.7	18.6
Ce	25.6	26.6	20.3	26	25	23.4	25.2	22.9	26.2	35.7	31.1	35.6	32.2	30.1
Pr	3.21	3.31	2.56	3.2	3.09	2.93	3.12	2.85	2.94	3.87	3.46	3.24	4.76	4.25
Nd	11.9	12.3	9.84	12	11.4	11.1	11.7	10.9	11.1	14	13.5	12.4	18.5	16.7
Sm	2.3	2.63	1.99	2.13	2.03	2.06	2.05	2.16	2.28	2.77	2.73	2.21	3.3	2.93
Eu	0.62	0.52	0.59	0.62	0.63	0.6	0.64	0.57	0.63	0.73	0.64	0.46	0.74	0.75
Gd	1.91	2.26	1.59	1.68	1.63	1.58	1.53	1.7	2.22	2.48	2.69	2.12	2.96	2.69
Tb	0.29	0.36	0.21	0.22	0.21	0.21	0.19	0.25	0.38	0.46	0.48	0.38	0.45	0.45
Dy	1.78	2.23	1.24	1.31	1.19	1.19	0.98	1.5	2.42	2.71	3.17	2.3	2.55	2.86
Ho	0.35	0.43	0.22	0.24	0.22	0.21	0.16	0.27	0.46	0.56	0.68	0.48	0.53	0.59
Er	0.94	1.18	0.57	0.63	0.58	0.55	0.41	0.74	1.46	1.75	2.15	1.56	1.54	1.81
Tm	0.16	0.2	0.09	0.1	0.08	0.08	0.06	0.12	0.24	0.28	0.37	0.25	0.25	0.3
Yb	0.9	1.28	0.55	0.6	0.51	0.51	0.35	0.75	1.51	1.9	2.57	1.67	1.66	1.95
Lu	0.14	0.21	0.1	0.11	0.08	0.09	0.06	0.12	0.26	0.31	0.42	0.28	0.26	0.3
Y	9.9	13	6.1	6.6	5.8	5.7	4.2	7.8	13.4	15.9	19.4	13.9	14.5	16.1
Cs	1.6	2.11	1.7	1.11	1.89	1.7	1.87	2.12	0.28	0.3	0.38	0.3	0.19	0.38
Rb	31.09	87.97	33.84	32.52	36.66	42.92	37.27	42.92	32.08	48.07	58.08	48.96	44.73	51.89

**Table 7.** *Cont.*

Sample No.	20HSD-Y1	20HSD-Y2	20HSD-Y3	20HSD-Y4	20HSD-Y5	20HSD-Y6	20HSD-Y7	20HSD-Y8	20HLD-Y1	20HLD-Y2	20HLD-Y3	20HLD-Y4	20HLD-Y5	20HLD-Y6
<i>Trace elements (ppm)</i>														
Ba	206	308	231	317	312	396	283	276	563	575	621	700	643	864
Th	2.32	2.92	1.75	2.17	1.81	1.65	1.55	2.03	3.66	4.73	5.11	6.22	3.93	4.38
U	0.48	0.67	0.49	0.42	0.49	0.52	0.46	0.49	0.98	1.47	1.73	1.2	0.98	1.1
Nb	4.65	6.51	2.73	3.57	3.2	3.78	3.46	3.46	7.12	8.08	10.6	7.98	7.07	8.58
Ta	0.38	0.68	0.35	0.2	0.32	0.32	0.31	0.45	0.62	0.86	1.25	0.87	0.78	0.93
Sr	178	58.58	261	272	262	273	289	266	221	258	318	167	221	163
Zr	74.98	41.58	81.33	89.33	87.4	88.87	95.04	90.9	158	158	178	141	154	166
Hf	2.93	1.85	3.46	3.3	3.64	3.33	3.76	4.11	6.64	7.2	8.28	6.14	7.11	7.24
Ti	779	185	1016	971	957	966	969	954	1959	1875	2029	1576	1927	2049
Cr	8.67	6.74	5.02	7.22	5.4	6.84	6.17	5.3	5.83	6.36	4.44	7.58	8.18	8.79
P	212	61.73	389	309	332	310	368	272	494	468	491	353	470	506
Mn	468	263	356	353	372	388	378	382	432	400	339	284	447	394
Ni	2.53	2.72	2.73	2.56	2.52	2.53	2.61	2.5	2.03	4.3	2.4	1.54	1.7	1.62
Zn	41.03	43.42	41.51	41.44	40.39	38.78	39.4	39.84	31.78	30.05	23.16	22.68	31.03	34.27
Sc	2.66	3.63	2.64	2.76	2.76	2.64	2.75	2.74	3.8	3.63	4.03	3.31	3.15	3.61
Ge	1.03	1.03	0.94	0.94	1.06	1.21	1.08	1.17	1	1.25	1.48	1.22	1.24	1.13
Co	1.98	1.82	2.33	2.08	1.92	1.95	2.04	2.06	3.24	3.08	3.57	2.35	3.23	2.97
Be	1.04	1.39	1.01	0.77	1.08	0.94	1.04	0.94	1.14	1.2	1.65	1.18	1.27	1.67
Li	36.63	27.42	46.86	35.56	39.6	36.91	36.27	31.91	4.13	3.36	3.47	3.43	2.75	4.56
Ga	16.38	17.42	17.13	16.41	17.4	16.61	16.63	16.76	11.74	13.42	16.34	12.17	13.02	14.3

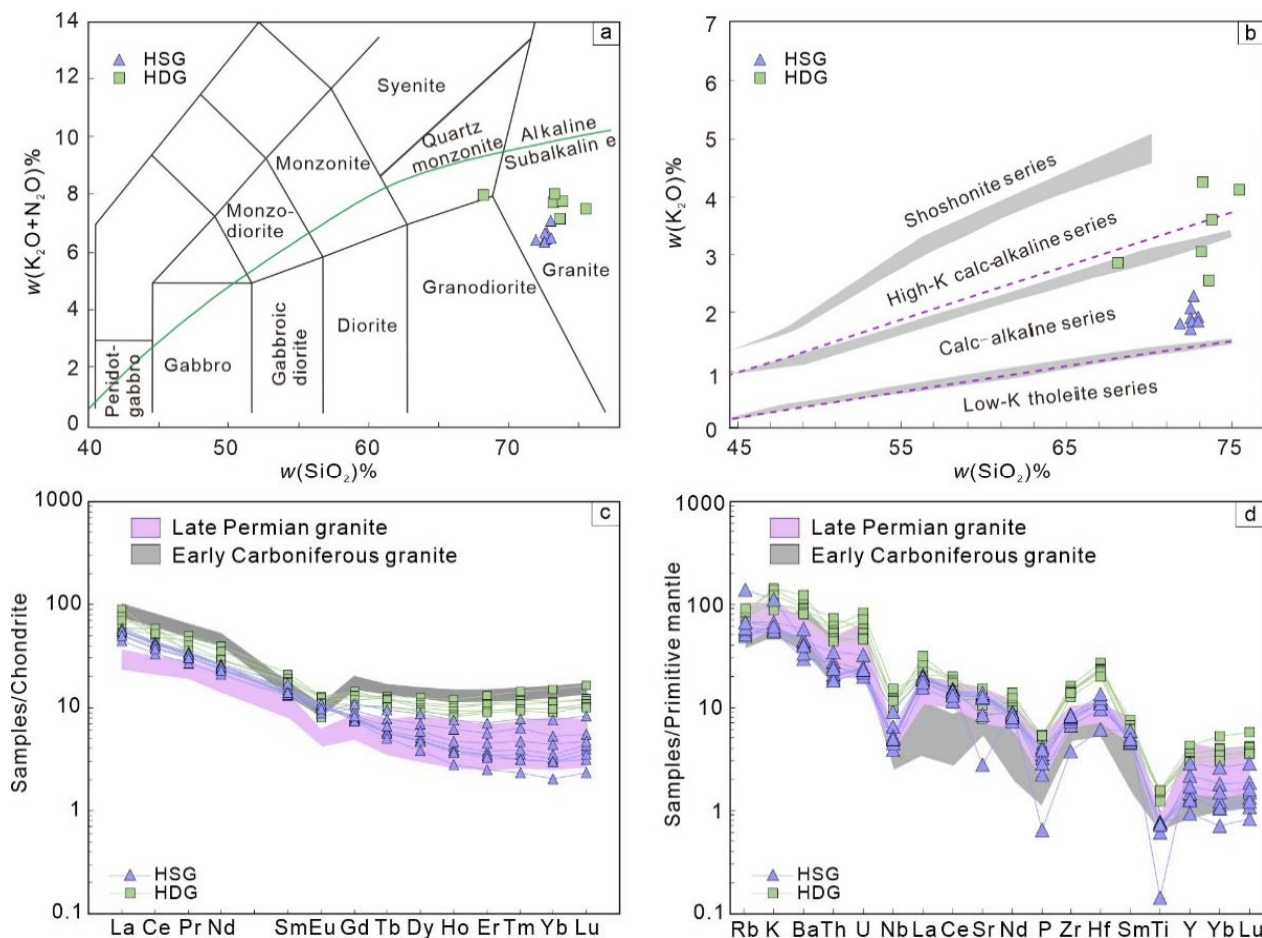


**Figure 7.** (a) Total alkali ( $\text{Na}_2\text{O} + \text{K}_2\text{O}$ ) versus silica ( $\text{SiO}_2$ ) (TAS) diagram, modified after Middlemost [86]. (b)  $\text{SiO}_2$  vs.  $\text{K}_2\text{O}$  diagram. (c) Chondrite-normalized REE distribution. (d) Primitive mantle-normalized trace element diagrams. Normalizing factors are from Sun and McDonough [87]. The data of Late Permian granite are from Muhtar et al. [49], and the data of Early Carboniferous granite are from Du et al. [88].

## 6. Discussion

### 6.1. Petrogenesis of Granites

The absence of amphibole, together with the high  $\text{SiO}_2$  (up to 75.47%), high total alkalinity ( $\text{K}_2\text{O} + \text{Na}_2\text{O} = 6.39 - 8.05\%$ ), and low  $\text{FeO}^\text{T}/\text{MgO}$  (2.4–3.4), suggests that the HSG and HDG experienced extensive magmatic fractionation [89]. The granite was previously interpreted as S-, I-, and A-types by different studies as it tends to have a similar major element and mineral composition to haplogranite [89,90]. The two plutons are relatively low in  $(\text{K}_2\text{O} + \text{Na}_2\text{O})/\text{CaO}$  and 10,000 Ga/Al, falling into the I- and S-type granite fields (Figure 8a). Notably, the A/CNK values (1.01–1.08) belong to peraluminous granites, in contrast to the S-type granites, which are usually strongly peraluminous with A/CNK values much higher than 1.1 [89,91]. Furthermore, the  $\text{P}_2\text{O}_5$  content (less than 0.2%) decreased with increasing  $\text{SiO}_2$  content (Figure 8b), thereby acting as a critical indicator for identifying I-type and S-type granites as apatite was more inclined to reach saturation in metaluminous and mildly peraluminous magmas ( $\text{A/CNK} < 1.1$ ) compared to strongly peraluminous melts [91,92]. Thus, the HSG and HDG are identified as I-type granites [91,93].

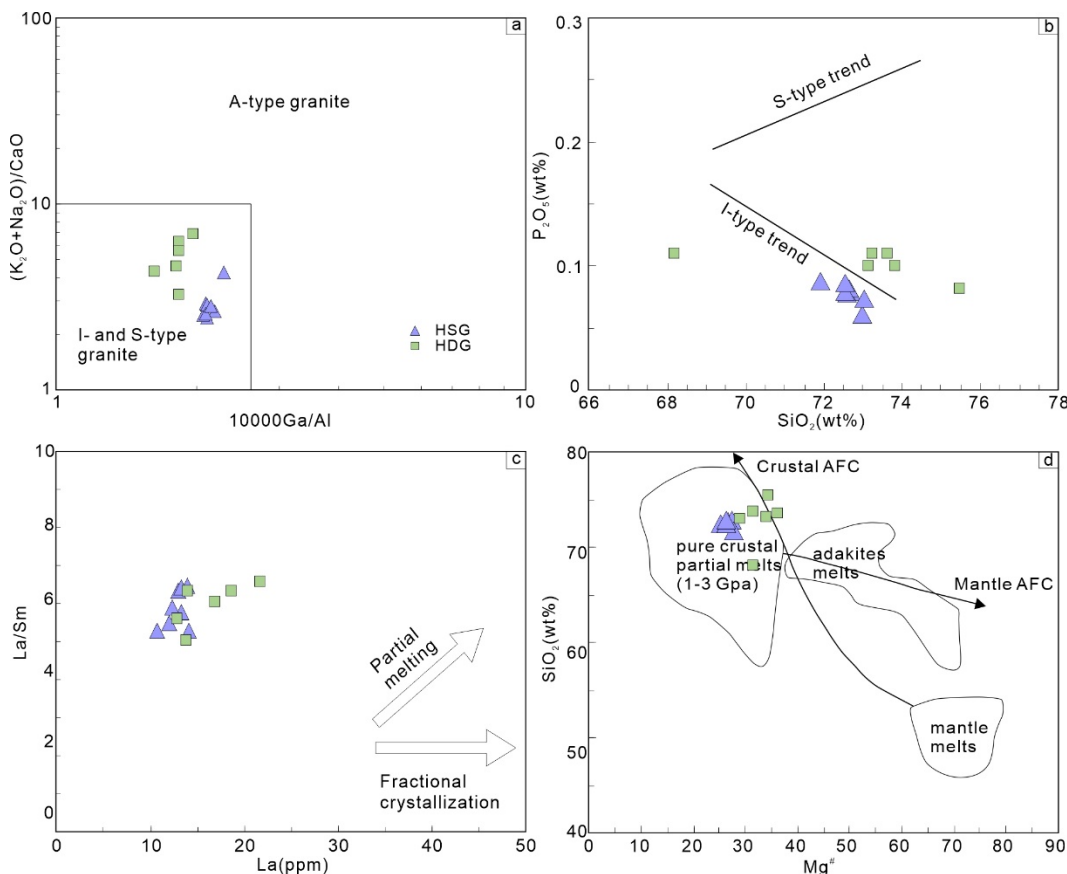


**Figure 8.** Geochemical affinity of the HSG and HDG. (a)  $(\text{K}_2\text{O} + \text{Na}_2\text{O})/\text{CaO}$  vs.  $10,000\text{Ga}/\text{Al}$ , after Whalen et al. [94]. (b)  $\text{SiO}_2$  vs.  $\text{P}_2\text{O}_5$  diagrams, after Chappell [91]. (c)  $\text{La}/\text{Sm}$  vs.  $\text{La}$ , after Chung et al. [95]. (d)  $\text{Mg}^{\#}$  vs.  $\text{SiO}_2$  diagram, after Gerdes et al. [96].

In general, magma sources proposed for I-type granites are (1) mafic to intermediate (meta)igneous rocks without sediments [97] or (2) mixed crustal-derived and mantle-derived magmas [98]. The samples from HSG and HDG show a positive correlation in the  $\text{La}$  vs.  $\text{La}/\text{Sm}$  diagram (Figure 8c), indicating that their compositional variations are mainly controlled by partial melting [95]. The samples show high  $\text{SiO}_2$  (up to 75.47%) and low  $\text{MgO}$  (less than 0.8%), indicating that they were generated by the partial melting of pure crustal material (Figure 8d). Furthermore, the ca. 347 Ma HDG is characterized by positive zircon  $\varepsilon\text{Hf}(t)$  values (10.5 to 12.2), relatively young  $T_{\text{DM2}}$  ages (552 to 655 Ma), and published data of lower  $(^{87}\text{Sr}/^{86}\text{Sr})_i$  ratios and higher  $\varepsilon\text{Nd}(t)$  of the Early Carboniferous [42], indicating that it originated from the re-melting of juvenile crustal-derived magma in a volcanic arc environment during the northward subduction of the Kanggur oceanic basin [88,99,100]. Nevertheless, the ca. 257 Ma HSG has higher positive zircon  $\varepsilon\text{Hf}(t)$  values (12.2 to 15.2), younger  $T_{\text{DM2}}$  ages (279.0 to 479.4 Ma), and published data of higher  $\varepsilon\text{Nd}(t)$  (5.42 to 7.12) of the Late Permian [49], indicating that it originated from the partial melting of thickened juvenile crust in a post-collisional environment [47,100].

## 6.2. Genesis of Apatite

### 6.2.1. Apatite from HSG

The U-Pb system of apatite from HSG is seemingly undisturbed as it recorded a single inverse isochron trend yielding  $249.1 \pm 1.8$  Ma ( $\text{MSWD} = 0.97$ ), which is consistent with the zircon U-Pb age of  $256.5 \pm 2.1$  Ma ( $\text{MSWD} = 0.89$ ). Meanwhile, the apatite grains from HSG do not record any textural evidence of deformation and recrystallization (Figure 5a). The slight enrichment in LREEs and MREEs, depletion in HREEs, and obvious negative Eu anomalies of apatite (Figure 9) correspond to those from classic granites of the Lachlan

Fold Belt showing little evidence of a metamorphic overprint [101,102]. As the substitution of variable valence elements in apatite is controlled by oxygen fugacity,  $\text{Ca}^{2+}$  in apatite is regularly replaced as it has a similar radius to  $\text{Eu}^{3+}$ ,  $\text{Mn}^{2+}$ , and  $\text{Ce}^{3+}$  [103]. Thus, the clustered  $\text{Ce}/\text{Ce}^*$  values (1.10–1.20) of apatite from HSG show a relatively stable crystallization environment (Figure 10a). Moreover, the remarkably high Mn (>2500 ppm) and low  $\text{Eu}/\text{Eu}^*$  (0.09–0.21) values imply that the apatite crystallized from magma (Figure 10b) [104]. This is consistent with the samples mostly being plotted within the I-type granite field (Figure 10c). Therefore, the mineralogy of homogeneous composition, similar geochronology, and clustered major and trace elements of apatite from HSG indicate that its grains were likely crystallized from I-type granite (Figure 10c). The lenticular morphology of the synkinematic granite is attributed to the crystallization in the plastic state during cooling.

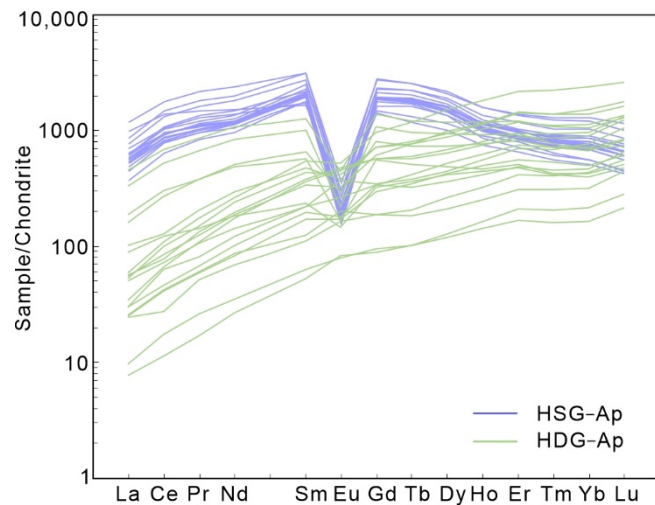


**Figure 9.** Chondrite-normalized REE patterns of apatite from HSG and HDG. The chondrite REE values are from Sun and McDonough [87].

### 6.2.2. Apatite from HDG

The U-Pb age of apatite from HDG records a single inverse isochron trend yielding  $248.1 \pm 4.0$  Ma ( $\text{MSWD} = 0.68$ ), which is obviously later than the zircon U-Pb age ( $347.3 \pm 2.5$  Ma,  $\text{MSWD} = 1.8$ ). Asynchronous U-Pb ages of zircon and apatite suggest that two tectono-magmatic events accompanied the unclosed U-Pb isotopic system. The deformation behavior of quartz and plagioclase from HDG indicates that they experienced deformation and recrystallization (Figure 2h–j). Moreover, the apatite grains with different colors in the EBSD images indicate that the composition of apatite grains from HDG underwent activation and migration (Figure 5c). Previous studies demonstrated that Y and LREEs can be released from apatite as REE-bearing phosphate mineral inclusions, wherein apatite interacts with low-salinity fluids [35,37,105–108]. The strong depletion in LREEs, enrichment in HREEs, and variable Eu anomalies of apatite suggested are obviously different from those of typical apatite from granite and thereby metasomatism (Figure 9) [101]. The scatter of  $\text{Ce}/\text{Ce}^*$  values (0.55–1.28) and LREE patterns of apatite grains from HDG show an unclosed transformation environment (Figure 10a) [37]. Low Mn (<860 ppm) and high  $\text{Eu}/\text{Eu}^*$  (0.30–1.34) values (Figure 10b) of apatite from HDG indicate that the later metasomatic fluid may yield an oxidizing system [37]. Thus, the heterogeneous composition, inconsistent geochronology of zircon and apatite, and scattered major and trace elements of apatite together indicate that the apatite grains crystallized from HDG show an obvious trend toward the low- and medium-grade metamorphic and metasomatic apatite fields (Figure 10c). The gneissic structure of HDG may be related to ductile deformation.

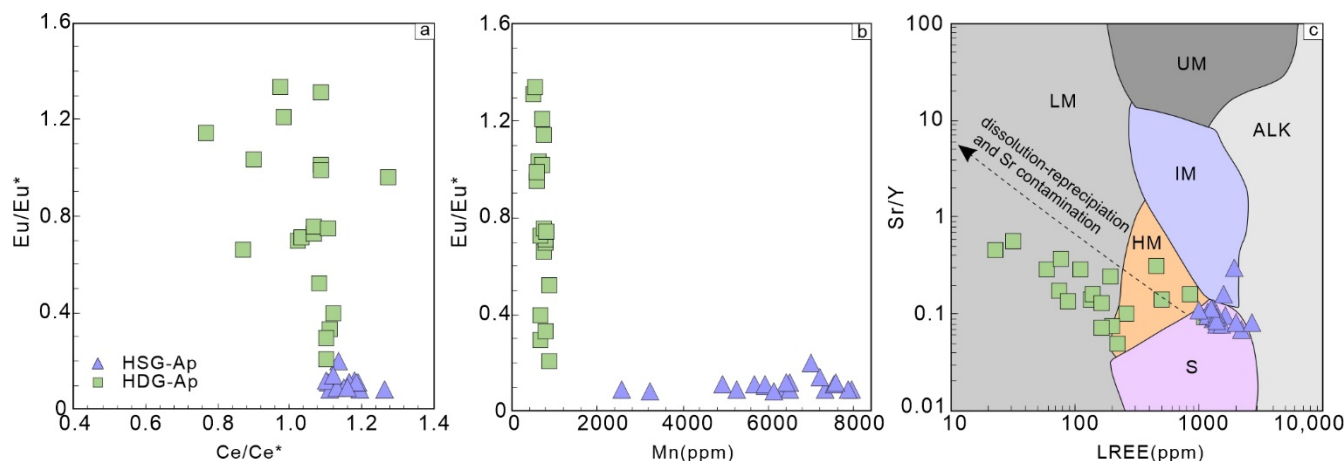


**Figure 10.** Biplots of apatite from the bedrock apatite database. (a) Eu/Eu\* vs. Ce/Ce\* in apatite. (b) Eu/Eu\* vs. Mn contents in apatite. (c) Sr/Y vs. ΣLREE (defined here as La-Nd), modified from O’Sullivan et al. [109]. Abbreviations for groups: ALK—alkali-rich igneous rocks; IM—mafic I-type granitoids and mafic igneous rocks; LM—low- and medium-grade metamorphic and metasomatic; HM—partial-melts/leucosomes/high-grade metamorphism; S—S-type granitoids and high aluminum saturation index (ASI) ‘felsic’ I-types; UM—ultramafic rocks including carbonatites, lherzolites, and pyroxenites.

### 6.3. Termination of the KDSZ Deformation

The orogenic gold deposits of the KDSZ, occurring in the Carboniferous strata with strong deformation, formed in the Late Permian to Early Triassic (e.g., Kanggur and Jinshan) [8,110]. Magmatic copper–nickel sulfide deposits of the KDSZ were formed in the Early Permian and underwent distinctly ductile deformation (e.g., Huangshandong) [9,10]. It can be inferred that the formation of the KDSZ is closely related to mineralization.

Based on field observations and measurements, previous studies have shown that the deformation process of the KDSZ can be divided into collisional N–S compression, post-collisional extension, and dextral strike slip [16,45,111,112]. The deformation of the KDSZ seems to have started with the subduction–accretion of the Kanggur ocean basin at the end of the Carboniferous [13,16,45]. Although different isotopic ages have been published (Table 8), including the U–Pb (zircon, niobium tantalite, and monazite), Re–Os (molybdenite), and Ar–Ar (biotite, muscovite, hornblende, plagioclase, and sericite) isotopic systems, the termination of the KDSZ deformation is still debated on Early Permian [13,17,18], Middle Permian [19–21], Late Permian [18,20], Early Triassic [14], or Middle Triassic (Table 8) [22]. Isotopic ages of typical tectono-magmatism in eastern Tianshan are shown in Table 8.

**Table 8.** Isotopic ages of typical tectono- magmatism in Eastern Tianshan.

No.	Name	Rocks/Ores	Deformation	Dated Minerals	Dating Methods	Ages (Ma)	References
1	Kanggur gold deposit	Mylonitized andesite	Apparently deformed	Zircon	LA-ICP-MS U-Pb	$338.0 \pm 1.7$	Muhtar et al. [8]
		Mylonitized dacite	Apparently deformed	Zircon	LA-ICP-MS U-Pb	$338.1 \pm 2.2$	Muhtar et al. [8]
		Mylonitized rhyolite	Apparently deformed	Zircon	LA-ICP-MS U-Pb	$332.4 \pm 2.8$	Muhtar et al. [8]
		Mylonitized granite porphyry	Apparently deformed	Zircon	LA-ICP-MS U-Pb	$342.6 \pm 1.9$	Muhtar et al. [8]
		Mylonitized quartz keratophyre	Apparently deformed	Whole rock	Ar-Ar plateau	$262.2 \pm 1.5$	Chen et al. [19]

**Table 8.** Cont.

No.	Name	Rocks/Ores	Deformation	Dated Minerals	Dating Methods	Ages (Ma)	References
	Quartz chlorite sericite mylonite	Apparently deformed	Whole rock	Ar-Ar plateau	$261.5 \pm 1.2$	Chen et al. [19]	
	Mylonitized pyroclastic rocks	Apparently deformed	Whole rock	Ar-Ar plateau	$262.9 \pm 1.4$	Chen et al. [19]	
	granitic mylonite	Apparently deformed	Whole rock	Ar-Ar plateau	$260.1 \pm 1.8$	Chen et al. [19]	
	Mylonitized gold ores	Apparently deformed	Sericite	Ar-Ar plateau	$253.9 \pm 1.8$	Chen et al. [20]	
	Mylonitized gold ores	Apparently deformed	Sericite	Ar-Ar plateau	$261.0 \pm 1.0$	Chen et al. [20]	
	Mylonitized gold ores	Apparently deformed	Sericite	Ar-Ar plateau	$252.5 \pm 1.7$	Chen et al. [20]	
	Mylonitized gold ores	Apparently deformed	Sericite	Ar-Ar plateau	$262.7 \pm 3.0$	Muhtar et al. [21]	
	Mylonitized gold ores	Apparently deformed	Sericite	Ar-Ar plateau	$263.4 \pm 2.9$	Muhtar et al. [21]	
	Mylonitized gold ores	Apparently deformed	Muscovite	Ar-Ar plateau	$256.0 \pm 1.0$	Liu et al. [113]	
2	Keziertage synkinematic granite	Gneissic biotite granite	Slightly deformed	Zircon	LA-ICP-MS U-Pb	$288.9 \pm 1.9$	Muhtar et al. [13]
		Biotite monzogranite	Slightly deformed	Zircon	LA-ICP-MS U-Pb	$291.5 \pm 1.7$	Muhtar et al. [13]
		K-feldspar granite	Slightly deformed	Zircon	LA-ICP-MS U-Pb	$287.9 \pm 3.1$	Muhtar et al. [13]
		Biotite quartz monzonite	Slightly deformed	Zircon	LA-ICP-MS U-Pb	$278.5 \pm 1.8$	Muhtar et al. [13]
		Gabbro	Slightly deformed	Zircon	LA-ICP-MS U-Pb	$278.1 \pm 2.3$	Muhtar et al. [13]
		Greisen diorite	Slightly deformed	Hornblende	Ar-Ar plateau	$276.5 + 1.6$	Wang et al. [17]
		Greisen diorite	Slightly deformed	Hornblende	Ar-Ar plateau	$276.0 + 4.0$	Wang et al. [17]
		Granite	Slightly deformed	Hornblende	Ar-Ar plateau	$276.5 \pm 1.6$	Wang et al. [18]
		Granite	Slightly deformed	Hornblende	Ar-Ar plateau	$272.2 \pm 1.5$	Wang et al. [18]
		Granite	Slightly deformed	Hornblende	Ar-Ar plateau	$278.4 \pm 1.5$	Wang et al. [18]
		Greisen diorite	Slightly deformed	Biotite	Ar-Ar plateau	$261.0 + 1.0$	Wang et al. [18]
		Greisen diorite	Slightly deformed	Biotite	Ar-Ar plateau	$253.9 \pm 2.3$	Wang et al. [18]
3	Huangshannan granite	Mylonitized muscovite granite	Apparently deformed	Zircon	LA-ICP-MS U-Pb	$259.9 \pm 1.4$	Tang et al. [114]
4	Shuangchagou granite	Mylonitized granodiorite	Apparently deformed	Zircon	LA-ICP-MS U-Pb	$252.4 \pm 2.9$	Zhou et al. [115]

**Table 8.** Cont.

No.	Name	Rocks/Ores	Deformation	Dated Minerals	Dating Methods	Ages (Ma)	References
5	Jingerquan pegmatite deposit	Pegmatite	Undeformed	Muscovite	Ar-Ar plateau	243.0 + 2.0	Chen et al. [22]
		Spodumene pegmatite	Undeformed	Niobium tantalite	LA-ICP-MS U-Pb	250.8 ± 1.0	Feng et al. [58]
		Peraluminous granite	Undeformed	Zircon	LA-ICP-MS U-Pb	250.0 ± 4.0	Muhtar et al. [47]
		Gabbro	Undeformed	Zircon	LA-ICP-MS U-Pb	248.7 ± 1.4	Liu et al. [48]
		Monzogabbro	Undeformed	Zircon	LA-ICP-MS U-Pb	250.7 ± 2.5	Liu et al. [48]
		Monzogabbro	Undeformed	Zircon	LA-ICP-MS U-Pb	247.0 ± 1.8	Liu et al. [48]
		Monzogabbro	Undeformed	Zircon	LA-ICP-MS U-Pb	247.6 ± 1.2	Liu et al. [48]
		Muscovite granite	Undeformed	Monazite	SIMS U-Th-Pb	252.9 ± 1.9	Liu et al. [48]
		Muscovite granite	Undeformed	Monazite	SIMS U-Th-Pb	246.0 ± 2.0	Liu et al. [48]
6	Donggebi molybdenum deposit	Porphyritic granite	Undeformed	Zircon	LA-ICP-MS U-Pb	234.6 ± 2.7	Sun et al. [116]
		Fine-grained granite	Undeformed	Zircon	LA-ICP-MS U-Pb	231.8 ± 2.4	Sun et al. [116]
		Ores	Undeformed	Molybdenite	Re-Os Isochron	234.0 ± 2.0	Sun et al. [116]
		Ores	Undeformed	Molybdenite	Re-Os Isochron	234.3 ± 1.6	Han et al. [117]
7	Baishan molybdenum deposit	Granite porphyry	Undeformed	Zircon	LA-ICP-MS U-Pb	228.1 ± 8.0	Zhang et al. [118]
		Ores	Undeformed	Molybdenite	Re-Os Isochron	224.8 ± 4.5	Zhang et al. [56]
8	Jinshan gold deposit	Mylonitized diorite	Apparently deformed	Zircon	LA-ICP-MS U-Pb	334.5 ± 4.7	Muhtar et al. [110]
		Auriferous quartz lode	Apparently deformed	Muscovite	Ar-Ar plateau	248.6 ± 0.8	Muhtar et al. [110]
		Auriferous quartz lode	Apparently deformed	Muscovite	Ar-Ar plateau	249.6 ± 0.9	Muhtar et al. [110]
9	Huangshandong synkinematic granite	Granodiorite	Slightly deformed	Zircon	LA-ICP-MS U-Pb	256.6 ± 1.1	This study
		Granodiorite	Slightly deformed	Apatite	LA-ICP-MS U-Pb	249.1 ± 1.8	This study
10	Huludong deformed granite	Monzogranite	Slightly deformed	Zircon	LA-ICP-MS U-Pb	347.3 ± 0.9	This study
		Monzogranite	Slightly deformed	Apatite	LA-ICP-MS U-Pb	248.1 ± 4.0	This study

As the U-Pb apatite system has a closure temperature of ca. 350–550 °C [31,38,40], it has been applied to constrain the shear zone deformation time [15,34] and metallogenetic process of magmatic hydrothermal deposits [35–37,43]. The closure temperature of the apatite U-Pb isotope system can be reduced to 190 °C if fluid is present [26,43]. In view of the deformation behavior of quartz and plagioclase during the ductile deformation [119,120], the deformation temperature of the KDSZ was estimated to be between 400 and 550 °C [50,51], corresponding to that of a typical ductile shear zone [121]. Thus, the deformation temperature of the KDSZ crossed the closure temperature of the apatite U-Pb isotopic system [40]. Furthermore, the apatite from HDG was metasomatized by fluid, indicating that the isotopic fingerprint was covered by metamorphism. Therefore,

we propose that the apatite age of ca. 248 Ma obtained in this study can be considered as the termination of the KDSZ deformation in eastern Tianshan, which can thus provide new constraints for the regional tectono-magmatic evolution (Figure 11) [122,123].

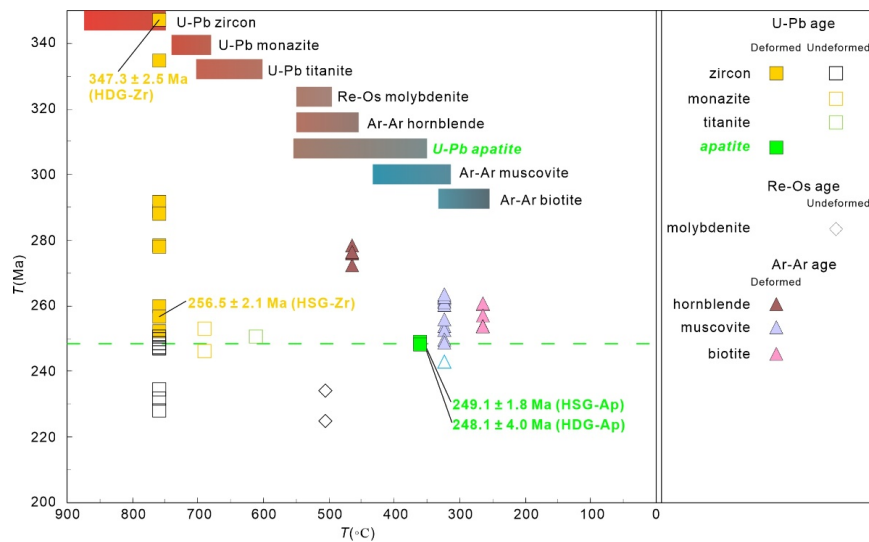


**Figure 11.** Isotopic ages and closure temperature of isotopic system. The closure temperature data of isotopic system are modified from Chew et al. [40].

However, what did the KDSZ experience from 347 to 248 Ma? The HDG formed at ca. 347 Ma is estimated to have invaded a depth of 15 km (Figure 12a), as the brittle-plastic transition of feldspar and quartz generally occurs at that depth. Combined with the minimum closure temperature ( $350^{\circ}\text{C}$ ) of apatite and the geothermal gradient ( $35^{\circ}\text{C}/\text{km}$ ), the HDG is estimated to have experienced an uplift of about 5 km from 347 to 248 Ma (Figure 12b), which is inferred to be related to the continuous evolution of the Paleo-Asian Ocean.

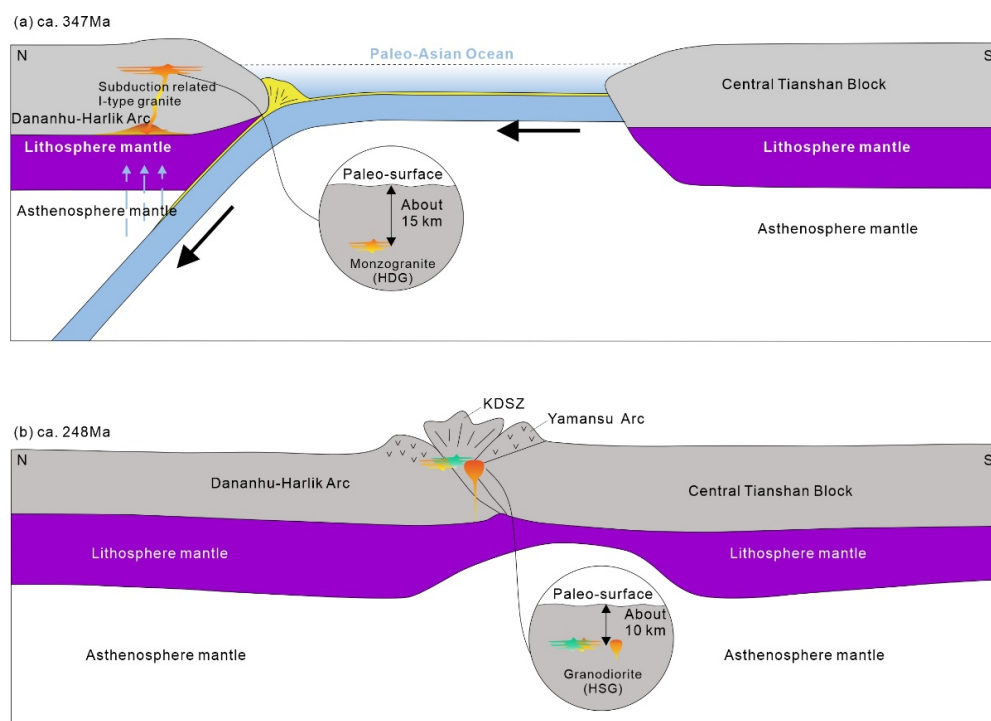


**Figure 12.** Schematic diagram of the crustal uplift during Early Carboniferous to Early Triassic.

## 7. Conclusions

- (1) The U-Pb age of apatite from HSG ( $249.1 \pm 1.8$  Ma, MSWD = 0.97) is identical to that of zircon ( $256.5 \pm 2.1$  Ma, MSWD = 0.89). Additionally, the U-Pb age of apatite from HDG ( $248.1 \pm 4.0$  Ma, MSWD = 0.68) is significantly later than that of zircon ( $347.3 \pm 2.5$  Ma, MSWD = 1.8).
- (2) The HSG and HDG have the geochemical characteristics of highly fractionated I-type granite petrogenesis. Moreover, their positive zircon  $\epsilon\text{Hf}(t)$  values and  $T_{\text{DM}2}$  ages indicate that the HSG originated from the re-melting of younger juvenile crustal-derived magma compared to HDG.
- (3) The apatite from HSG is characterized by high Mn, low Eu/Eu\*, slight enrichment in MREEs, and obvious negative Eu anomalies, indicating a typical magmatic origin. In contrast, the apatite from HDG is characterized by low Mn, high Eu/Eu\*, and depletion in LREEs, demonstrating that it experienced fluid metasomatism with a metamorphic overprinting.
- (4) The apatite U-Pb age (ca. 248.1 Ma) is interpreted as the Early Triassic tectono-magmatism event, which not only corresponds to the magmatism and mineralization in the Jingerquan area, but also represents the termination of KDSZ deformation in eastern Tianshan.

**Author Contributions:** Conceptualization, T.L. and P.L.; formal analysis, P.L. and Y.-G.F.; investigation, P.L. and T.-Y.Z.; resources, G.C. and Z.-X.Z.; writing—original draft preparation, P.L.; writing—review and editing, T.L. and Y.-G.F.; supervision, T.L.; funding acquisition, G.C. All authors have read and agreed to the published version of the manuscript.

**Funding:** This research was funded by the second Tibetan Plateau Scientific Expedition and Research (2019QZKK0806), the National Key R & D project of China (2018YFC0604001–04) and the Project of Xinjiang Natural Science Youth Fund (2020D01B51).

**Data Availability Statement:** The raw/processed data required to reproduce these findings cannot be shared at this time as the data also forms part of an ongoing study.

**Acknowledgments:** We thank Changzhi Wu and Mengxi Wang from the Chang'an University for their discussion on primary manuscript. We also thank Qiong Han and Liuyuan Jin of Xinjiang Geological Survey Academy for their assistance during fieldwork.

**Conflicts of Interest:** The authors declare that they have no known competing financial interest or personal relationships that could have appeared to influence the work reported in this paper.

## References

1. Sengör, A.M.C.; Natal'in, B.A.; Burtman, V.S. Evolution of the Altai tectonic collage and Palaeozoic crustal growth in Eurasia. *Nature* **1993**, *364*, 299–307. [[CrossRef](#)]
2. Windley, B.F.; Alexeiev, D.; Xiao, W.J.; Kröner, A.; Badarch, G. Tectonic models for accretion of the Central Asian Orogenic Belt. *J. Geol. Soc. Lond.* **2007**, *164*, 31–47. [[CrossRef](#)]
3. Allen, M.; Windley, B.; Zhang, C. Palaeozoic collisional tectonics and magmatism of the Chinese Tien Shan, central Asia. *Tectonophysics* **1993**, *220*, 89–115. [[CrossRef](#)]
4. Khain, E.V.; Bibikova, E.V.; Kröner, A.; Zhuravlev, D.Z.; Sklyarov, E.V.; Fedotova, A.A.; Kravchenko-Berezhnoy, I.R. The most ancient ophiolite of the Central Asian fold belt: U-Pb and Pb-Pb zircon ages for the Dunzhugur Complex, Eastern Sayan, Siberia, and geodynamic implications. *Earth Planet. Sci. Lett.* **2002**, *199*, 311–325. [[CrossRef](#)]
5. Xiao, W.J.; Han, C.M.; Yuan, C.; Sun, M.; Lin, S.F.; Chen, H.L.; Li, Z.L.; Li, J.L.; Sun, S. Middle Cambrian to Permian subduction-related accretionary orogenesis of Northern Xinjiang, NW China: Implications for the tectonic evolution of central Asia. *J. Asian Earth Sci.* **2008**, *32*, 102–117. [[CrossRef](#)]
6. Xiao, W.J.; Kröner, A.; Windley, B.F. Geodynamic evolution of Central Asia in the Paleozoic and Mesozoic: Int. *J. Earth Sci.* **2009**, *98*, 1185–1188. [[CrossRef](#)]
7. Xiao, W.J.; Windley, B.F.; Sun, S.; Li, J.L.; Huang, B.C.; Han, C.M.; Yuan, C.; Sun, M.; Chen, H.L. A tale of amalgamation of three Permo-Triassic collage systems in central Asia: Oroclines, sutures, and terminal accretion. *Annu. Rev. Earth Planet. Sci.* **2015**, *43*, 477–507. [[CrossRef](#)]
8. Muhtar, M.N.; Wu, C.Z.; Brzozowski, M.J.; Li, P.; Yuan, X.C.; Wang, S.M.; Zhi, J.; Jiang, Y.H. Geochronology, geochemistry, and Sr-Nd-Pb-Hf-S isotopes of the wall rocks of the Kanggur gold polymetallic deposit, Chinese North Tianshan: Implications for petrogenesis and sources of ore-forming materials. *Ore Geol. Rev.* **2020**, *125*, 103688. [[CrossRef](#)]

9. Wu, C.Z.; Xie, S.W.; Gu, L.X.; Samson, I.M.; Yang, T.; Lei, R.X.; Zhu, Z.Y.; Dang, B. Shear zone-controlled post-magmatic ore formation in the Huangshandong Ni-Cu sulfide deposit, NW China. *Ore Geol. Rev.* **2018**, *100*, 545–560. [[CrossRef](#)]
10. Wang, S.M.; Wu, C.Z.; Muhtar, M.N.; Lei, R.X.; Brzozowski, M.J. Mobilization of ore-forming metals during post-magmatic hydrothermal overprinting of the Huangshandong Ni–Cu sulfide deposit, Eastern Tianshan, NW China. *Ore Geol. Rev.* **2021**, *137*, 104315. [[CrossRef](#)]
11. Branquet, Y.; Gumiiaux, C.; Sizaret, S.; Barbanson, L.; Wang, B.; Cluzel, D.; Li, G.; Delaunay, A. Synkinematic mafic/ultramafic sheeted intrusions: Emplacement mechanism and strain restoration of the Permian Huangshan Ni-Cu ore belt (Eastern Tianshan, NW China). *J. Asian Earth Sci.* **2012**, *56*, 240–257. [[CrossRef](#)]
12. Wang, B.; Cluzel, D.; Jahn, B.M.; Shu, L.S.; Chen, Y.; Zhai, Y.Z.; Branquet, Y.; Barbanson, L.; Sizaret, S. Late Paleozoic pre- and syn- Kinematic plutons of the Kanggur-Huangshan shear zone: Inference on the tectonic evolution of the eastern Chinese north Tianshan. *Am. J. Sci.* **2014**, *314*, 43–79. [[CrossRef](#)]
13. Muhtar, M.N.; Gan, K.; Wang, S.M.; Gu, L.X.; Lei, R.X.; Santosh, M.; Wu, C.Z. Late Paleozoic tectonic transition from subduction to post-collisional extension in Eastern Tianshan, Central Asian Orogenic Belt. *The Geol. Soc. Am. Bull.* **2020**, *132*, 1756–1774. [[CrossRef](#)]
14. Muhtar, M.N.; Wu, C.Z.; Brzozowski, M.J.; Santosh, M.; Tian, R.S.; Xie, G.A.; Zhang, W.F.; Lei, R.X.; Xiao, W.J. Timing and spatial variation of deformation along the Kanggur-Huangshan shear zone in the Chinese Tianshan: Implications for regional differential uplift and mineralization. *GSA Bull.* **2022**. [[CrossRef](#)]
15. Margaret, L.; Odium, D.F.S. Geochronologic constraints on deformation and metasomatism along an exhumed mylonitic shear zone using apatite U-Pb, geochemistry, and microtextural analysis. *Earth Planet. Sc. Lett.* **2020**, *538*, 116177. [[CrossRef](#)]
16. Guo, L.; Ren, Y. The structural feature and deformation stage of the Huangshan ductile shear belt in the Huangshandong. *XinJiang Geol.* **2012**, *30*, 34–37. (In Chinese)
17. Wang, Y.; Li, J.Y.; Li, W.Q.  $^{40}\text{Ar}$ - $^{39}\text{Ar}$  chronological evidence of dextral shear and tectonic evolution of the eastern Tianshan orogenic belt. *Xinjiang Geol.* **2002**, *20*, 315–319. (In Chinese)
18. Wang, Y.; Li, J.Y.; Sun, G.H. Postcollisional Eastward Extrusion and Tectonic Exhumation along the Eastern Tianshan Orogen, Central Asia: Constraints from Dextral Strike-Slip Motion and  $^{40}\text{Ar}$ / $^{39}\text{Ar}$  Geochronological Evidence. *J. Geol.* **2008**, *116*, 599–618. [[CrossRef](#)]
19. Chen, W.; Sun, Y.; Zhang, Y.; Xiao, W.J.; Wang, Y.T.; Wang, Q.L.; Jiang, L.F.; Yang, J.T.  $^{40}\text{Ar}$ / $^{39}\text{Ar}$  Geochronology of the Qiugemingtashi-Huangshan Ductile Shear Zone in East Tianshan, Xinjiang, NW China. *Acta Geol. Sin.* **2005**, *79*, 791–804. (In Chinese)
20. Chen, W.; Zhang, Y.; Qin, K.Z.; Wang, Q.L.; Wang, Y.T.; Liu, X.Y. Study on the age of the shear zone-type gold deposit of East Tianshan, Xinjiang, China. *Acta Petrol. Sin.* **2007**, *23*, 2007–2016. (In Chinese)
21. Muhtar, M.N.; Wu, C.Z.; Brzozowski, M.J.; Lei, R.X.; Feng, Z.J.; Chen, B.Y.; Jiang, Y.H. Sericite  $^{40}\text{Ar}$ / $^{39}\text{Ar}$  dating and S-Pb isotope composition of the Kanggur gold deposit: Implications for metallogenesis of late Paleozoic gold deposits in the Tianshan, central Asian Orogenic Belt. *Ore Geol. Rev.* **2021**, *131*, 104056. [[CrossRef](#)]
22. Chen, Z.H.; Wang, D.H.; Gong, Y.F.; Chen, Y.C.; Chen, S.P.  $^{40}\text{Ar}$ / $^{39}\text{Ar}$  isotope dating of muscovite from Jingerquan pegmatite rare metal deposit in Hami, Xinjiang, and its geological significance. *Miner. Depos.* **2006**, *25*, 470–476. (In Chinese)
23. Bingen, B.; Austrheim, H.; Whitehouse, M. Ilmenite as a source for zirconiumduring high-grade metamorphism? Textural evidence from the Caledonides of W. Norway and implications for zircon geochronology. *J. Petrol.* **2001**, *42*, 355–375. [[CrossRef](#)]
24. Hoskin, P.W.O.; Schaltegger, U. The composition of zircon and igneous and metamorphic petrogenesis. *Rev. Mineral. Geochem.* **2003**, *53*, 27–62. [[CrossRef](#)]
25. Lei, W.; Shi, G.; Santosh, M.; Ng, Y.; Liu, Y.; Wang, J.; Xie, G.; Ju, Y. Trace element features of hydrothermal and inherited igneous zircon grains in mantle wedge environment: A case study from the Myanmar jadeitite. *Lithos* **2016**, *266–267*, 16–27. [[CrossRef](#)]
26. Kusebauch, C.; John, T.; Whitehouse, M.J.; Klemme, S.; Putnis, A. Distribution of halogens between fluid and apatite during fluid-mediated replacement processes. *Geochim. Cosmochim. Acta* **2015**, *170*, 225–246. [[CrossRef](#)]
27. Ansberque, C.; Mark, C.; Caulfield, J.T.; Chew, D.M. Combined in-situ determination of halogen (F, Cl) content in igneous and detrital apatite by SEM-EDS and LA-Q-ICPMS: A potential new provenance tool. *Chem. Geol.* **2019**, *524*, 406–420. [[CrossRef](#)]
28. Glorie, S.; March, S.; Nixon, A.; Meeuws, F.; O’Sullivan, G.J.; Chew, D.M.; Kirkland, C.L.; Konopelko, D.; De, G.J. Apatite U-Pb dating and geochemistry of the Kyrgyz South Tian Shan (Central Asia): Establishing an apatite fingerprint for provenance studies. *Geosci. Front.* **2020**, *11*, 2003–2015. [[CrossRef](#)]
29. Ansberque, C.; Chew, D.M.; Drost, K. Apatite fission-track dating by LA-Q-ICP-MS imaging. *Chem. Geol.* **2021**, *560*, 119977. [[CrossRef](#)]
30. Green, P. On the thermo-tectonic evolution of Northern England: Evidence from fission-track analysis. *Geol. Mag.* **1986**, *123*, 493–506. [[CrossRef](#)]
31. Chew, D.M.; Sylvester, P.J.; Tubrett, M.N. U-Pb and Th-Pb dating of apatite by LA-ICPMS. *Chem. Geol.* **2011**, *280*, 200–216. [[CrossRef](#)]
32. Tamer, M.; Ketcham, R. Is low-temperature fission-track annealing in apatite a thermally controlled process? *Geochem. Geophys. Geosystems* **2020**, *21*, e2019GC008877. [[CrossRef](#)]
33. Zhou, H.Y.; Geng, J.Z.; Cui, Y.R.; Li, H.K.; Li, H.M. In Situ U-Pb Dating of Apatite Using LA-MC-ICP-MS. *Acta Geosci. Sin.* **2012**, *33*, 857–864. (In Chinese)

34. Ribeiro, B.V.; Lagoeiro, L.; Faleiros, F.M.; Hunter, N.J.R.; Queiroga, G.; Raveggi, M.; Cawood, P.A.; Finch, M.; Campanha, G.A.C. Strain localization and fluid-assisted deformation in apatite and its influence on trace elements and U-Pb systematics. *Earth Planet. Sci. Lett.* **2020**, *545*, 116421. [[CrossRef](#)]
35. Mao, M.; Rukhlov, A.S.; Rowins, S.M.; Spence, J.; Coogan, L.A. Apatite trace element compositions: A robust new tool for mineral exploration. *Econ. Geol.* **2016**, *111*, 1187–1222. [[CrossRef](#)]
36. Tang, P.; Tang, J.; Wang, Y.; Lin, B.; Leng, Q.; Zhang, Q.; He, L.; Zhang, Z.; Sun, M.; Wu, C.; et al. Genesis of the Lakang'e porphyry Mo (Cu) deposit, Tibet: Constraints from geochemistry, geochronology, Sr-Nd-Pb-Hf isotopes, zircon and apatite. *Lithos* **2020**. [[CrossRef](#)]
37. Zhang, F.; Li, W.; White, N.C.; Zhang, L.; Qiao, X.; Yao, Z. Geochemical and isotopic study of metasomatic apatite: Implications for gold mineralization in Xindigou, northern China. *Ore Geol. Rev.* **2020**, *127*, 103853. [[CrossRef](#)]
38. Chamberlain, K.R.; Bowring, S.A. Apatite-Feldspar U-Pb thermochronometer: A reliable, mid-range (450 °C), diffusion-controlled system. *Chem. Geol.* **2000**, *172*, 173–200. [[CrossRef](#)]
39. Schoene, B.; Bowring, S.A. Determining accurate temperature-time paths from U-Pb thermochronology: An example from the Kaapvaal craton, southern Africa. *Geochim. Cosmochim. Acta* **2007**, *71*, 165–185. [[CrossRef](#)]
40. Chew, D.M.; Petrus, J.A.; Kamber, B.S. U-Pb LA-ICPMS dating using accessory mineral standards with variable common Pb. *Chem. Geol.* **2014**, *363*, 185–199. [[CrossRef](#)]
41. Chew, D.M.; Spikings, R.A. Geochronology and thermochronology using apatite: Time and temperature, lower crust to surface. *Elements* **2015**, *11*, 189–194. [[CrossRef](#)]
42. Du, J.G.; Wang, G.W.; Jia, L.H. In situ major and trace element compositions of apatites from Luanchuan orecluster: Implications for porphyry Mo mineralization. *Ore Geol. Rev.* **2019**, *115*, 103174. [[CrossRef](#)]
43. Cao, M.; Evans, N.J.; Qin, K.; Danišík, M.; Li, G.; McInnes, B.I.A. Open apatite Sr isotopic system in low-temperature hydrous regimes. *J. Geophys. Res. Solid Earth* **2019**, *124*, 11192–11203. [[CrossRef](#)]
44. Li, P.; Liang, T.; Feng, Y.G.; Zhao, T.Y.; Feng, J.; Han, Q.; Li, Y.; Jin, L.Y. Zircon U-Pb and molybdenite Re-Os geochronology and geochemistry of the Tieling deposit in the Eastern Tianshan, NW China: Insights into the timing of mineralization and tectonic setting. *Ore Geol. Rev.* **2022**, *141*, 104656. [[CrossRef](#)]
45. Dong, L.H.; Wang, K.Z.; Zhu, Z.X.; Zhao, T.Y.; Zheng, J.X.; Xu, S.Q. The relationship between the characteristics of the large-scale deformation structure and the metallogenic processes in Xinjiang. *Geol. China* **2013**, *40*, 1552–1568. (In Chinese)
46. Li, W.Q.; Dong, F.R.; Zhou, R.H. Ophiolite discovered in Kangurtag region and its characteristics. *Xinjiang Geol.* **2000**, *18*, 121–128. (In Chinese)
47. Muhtar, M.N.; Wu, C.Z.; Santosh, M.; Lei, R.X.; Feng, Y.; Yang, T.; Ye, H.; Gu, L.X.; Yang, G. Peraluminous granitoid magmatism from isotopically depleted sources: The case of Jing'erquanbei pluton in Eastern Tianshan, Northwest China. *Geol. J.* **2018**, *55*, 117–132. [[CrossRef](#)]
48. Liu, S.Y.; Wang, R.; Jeon, H.; Hou, Z.; Xue, Q.; Zhou, L.; Chen, S.; Zhang, Z.; Xi, B. Indosinian magmatism and rare metal mineralization in East Tianshan orogenic belt: An example study of Jingerquan Li-Be-Nb-Ta pegmatite deposit. *Ore Geol. Rev.* **2020**, *116*, 103265. [[CrossRef](#)]
49. Muhtar, M.N.; Wu, C.; Brzozowski, M.J.; Lei, R.X.; Wang, M.; Xiao, W. Permian ridge subduction-related magmatism in the Eastern Tianshan: Implications for the evolution of the southern Altaiids. *Lithos* **2022**, *428–429*, 106815. [[CrossRef](#)]
50. Xu, X.W.; Ma, T.L.; Sun, L.Q.; Cai, X.P. Characteristics and dynamic origin of the large-scale Jiaoluotage ductile compressional zone in the eastern Tianshan Mountains, China. *J. Struct. Geol.* **2003**, *25*, 1901–1915. [[CrossRef](#)]
51. Hu, J.; Yu, X.Q.; Lu, Z.Y.; Zeng, Y.; Liu, X.; Wang, Z.F. Ductile-compressional deformation of Kanggur ductile deformation zone in the Eastern Tianshan Mountains: A case study of Huangshandong area of Hami City. *Earth Sci.* **2020**, *45*, 1636–1652. (In Chinese)
52. Wang, K.; Ji, W.H.; Meng, Y.; Zhang, X.; Zhu, X.H.; Li, P. Deformation in Eastern Tianshan orogenic belt: Response to the final stage of accretionary orogenesis. *Geotecton. Metallog.* **2019**, *43*, 894–910. (In Chinese)
53. Mao, Y.J.; Qin, K.Z.; Tang, D.M.; Feng, H.Y.; Xue, S.C. Crustal contamination and sulfide immiscibility history of the Permian Huangshannan magmatic Ni-Cu sulfide deposit, East Tianshan, NW China. *J. Asian Earth Sci.* **2016**, *129*, 22–37. [[CrossRef](#)]
54. Deng, Y.F.; Yuan, F.; Hollings, P.; Song, X.Y.; Zhou, T.F.; Fu, B.; Denysyn, S.; Zhao, B.B. Magma generation and sulfide saturation of Permian mafic-ultramafic intrusions from the western part of the Northern Tianshan in NW China: Implications for Ni-Cu mineralization. *Miner. Depos.* **2020**, *55*, 515–534. [[CrossRef](#)]
55. Li, P.; Liang, T.; Feng, Y.G.; Zhao, T.Y.; Tian, J.T.; Li, D.H.; Li, J.; Chen, G.; Wu, C.Z. The Metallogeny of the Lubei Ni-Cu-Co sulfide deposit in Eastern Tianshan, NW China: Insights from petrology and Sr-Nd-Hf isotopes. *Front. Earth Sci.* **2021**, *9*, 648122. [[CrossRef](#)]
56. Zhang, L.C.; Xiao, W.J.; Qin, K.Z.; Qu, W.J.; Du, A.D. Re-Os isotopic dating of molybdenite and pyrite in the Baishan Mo-Re deposit, eastern Tianshan, NW China, and its geological significance. *Miner. Depos.* **2005**, *39*, 960–969. [[CrossRef](#)]
57. Wu, Y.S.; Zhou, K.F.; Li, N.; Chen, Y.J. Zircon U-Pb dating and Sr-Nd-Pb-Hf isotopes of the ore-associated porphyry at the giant Donggebi Mo deposit, Eastern Tianshan, NW China. *Ore Geol. Rev.* **2017**, *81*, 794–807. [[CrossRef](#)]
58. Feng, Y.G.; Liang, T.; Lei, R.X.; Ju, M.H.; Zhang, Z.L.; Gao, J.G.; Zhou, Y.; Wu, C.Z. Relationship Between Undercooling and Emplacement of Rare-element Pegmatites-Thinking Based on Field Observations and Pegmatite Geochronology. *J. Earth Sci. Environ.* **2021**, *43*, 100–116. [[CrossRef](#)]

59. Wang, Y.H.; Xue, C.J.; Liu, J.J.; Wang, J.P.; Yang, J.T.; Zhang, F.F.; Zhao, Z.N.; Zhao, Y.J.; Liu, B. Early Carboniferous adakitic rocks in the area of the Tuwu deposit, eastern Tianshan, NW China: Slab melting and implications for porphyry copper mineralization. *J. Asian Earth Sci.* **2015**, *103*, 332–349. [[CrossRef](#)]
60. Wang, Y.H.; Zhang, F.F.; Liu, J.J. The genesis of the ores and intrusions at the Yuhai Cu-Mo deposit in eastern Tianshan, NW China: Constraints from geology, geochronology, geochemistry, and Hf isotope systematics. *Ore Geol. Rev.* **2016**, *77*, 312–331. [[CrossRef](#)]
61. Wang, Y.H.; Zhang, F.F.; Liu, J.J.; Que, C.Y. Genesis of the Fuxing porphyry Cu deposit in Eastern Tianshan, China: Evidence from fluid inclusions and C-H-O-S-Pb isotope systematics. *Ore Geol. Rev.* **2016**, *79*, 46–61. [[CrossRef](#)]
62. Mao, Q.G.; Wang, J.B.; Yu, M.J.; Ao, S.J.; Deng, X.H.; Lü, X.Q.; Li, Y.C. Re-Os and U-Pb geochronology for the Xiaorequanzi VMS deposit in the Eastern Tianshan, NW China: Constraints on the timing of mineralization and stratigraphy. *Ore Geol. Rev.* **2020**, *122*, 103473. [[CrossRef](#)]
63. Cheng, X.H.; Yang, F.Q.; Zhang, R.; Xu, Q.F.; Li, N. Metallogenesis and fluid evolution of the Huangtupo Cu-Zn deposit, East Tianshan, Xinjiang, NW China: Constraints from ore geology, fluid inclusion geochemistry, H-O-S isotopes, and U-Pb zircon, Re-Os chalcopyrite geochronology. *Ore Geol. Rev.* **2020**, *121*, 103469. [[CrossRef](#)]
64. Deng, X.H.; Wang, J.B.; Santosh, M.; Li, Y.C.; Wang, Y.W.; Mao, Q.G.; Long, L.L.; Chen, X. New  $^{40}\text{Ar}/^{39}\text{Ar}$  ages from the Kalatag district in the Eastern Tianshan, NW China: Constraints on the timing of Cu mineralization and stratigraphy. *Ore Geol. Rev.* **2018**, *100*, 250–262. [[CrossRef](#)]
65. Du, L.; Long, X.; Yuan, C.; Zhang, Y.; Huang, Z.; Sun, M.; Zhao, G.; Xiao, W. Early Paleozoic dioritic and granitic plutons in the Eastern Tianshan Orogenic Belt, NW China: Constraints on the initiation of a magmatic arc in the southern Central Asian Orogenic Belt. *J. Asian Earth Sci.* **2018**, *153*, 139–153. [[CrossRef](#)]
66. Zhao, L.D.; Chen, H.Y.; Hollings, P.; Han, J.S. Late Paleozoic magmatism and metallogenesis in the Aqishan-Yamansu belt, Eastern Tianshan: Constraints from the Bailingshan intrusive complex. *Gondwana Res.* **2019**, *65*, 68–85. [[CrossRef](#)]
67. Long, X.P.; Wu, B.; Sun, M.; Yuan, C.; Xiao, W.J.; Zuo, R. Geochronology and geochemistry of Late Carboniferous dykes in the Aqishan-Yamansu belt, eastern Tianshan: Evidence for a post-collisional slab breakoff. *Geosci. Front.* **2020**, *11*, 347–362. [[CrossRef](#)]
68. Zhang, W.F.; Chen, H.Y.; Peng, L.H.; Zhao, L.D.; Lu, W.J.; Zhang, Z.J.; Yang, J.T.; Sun, J. Ore genesis of the Duotoushan Fe-Cu deposit, Eastern Tianshan, NW China: Constraints from ore geology, mineral geochemistry, fluid inclusion and stable isotopes. *Ore Geol. Rev.* **2018**, *100*, 401–421. [[CrossRef](#)]
69. Han, J.S.; Chen, H.Y.; Jiang, H.J.; Zhao, L.D.; Zhang, W.F.; Lai, C.K. Genesis of the Paleozoic Aqishan-Yamansu arc-basin system and Fe (-Cu) mineralization in the Eastern Tianshan, NW China. *Ore Geol. Rev.* **2019**, *105*, 55–70. [[CrossRef](#)]
70. Hu, X.; Chen, H.; Huang, X.; Zhang, W. Texture and composition of magnetite in the Duotoushan deposit, NW China: Implications for ore genesis of Fe-Cu deposits. *Mineral. Mag.* **2020**, *84*, 398–411. [[CrossRef](#)]
71. Mao, Q.; Ao, S.; Windley, B.F.; Song, D.; Sang, M.; Tan, Z.; Wang, H.; Li, R.; Xiao, W. Late Paleozoic southward migration of the Dananhu arc in the Eastern Tianshan (NW China). *Earth Space Sci.* **2022**, *9*. [[CrossRef](#)]
72. Ludwig, K.R. *User's Manual for Isoplot/Ex. Version 3.00: A Geochronological Toolkit for Microsoft Excel*; Berkeley Geochronology Center Special Publication: Berkeley, CA, USA, 2003; pp. 1–77.
73. Liu, Y.S.; Hu, Z.C.; Zong, K.Q.; Gao, C.G.; Gao, S.; Xu, J.; Chen, H.H. Reappraisal and refinement of zircon U-Pb isotope and trace element analyses by LA-ICP-MS. *Chin. Sci. Bull.* **2010**, *55*, 1535–1546. [[CrossRef](#)]
74. Cochrane, R.; Spikings, R.A.; Chew, D.; Wotzlaw, J.F.; Chiaradia, M.; Tyrrell, S.; Schaltegger, U.; Van der Lelij, R. High temperature ( $>350^\circ\text{C}$ ) thermochronology and mechanisms of Pb loss in apatite. *Geochim. Cosmochim. Acta* **2014**, *127*, 39–56. [[CrossRef](#)]
75. Schoene, B.; Bowring, S.A. U-Pb systematics of the McClure Mountain syenite: Thermochronological constraints on the age of the  $^{40}\text{Ar}/^{39}\text{Ar}$  standard MMhb. *Contrib. Mineral. Petrol.* **2006**, *151*, 615–630. [[CrossRef](#)]
76. Barfod, G.H.; Krogstad, E.J.; Frei, R.; Albarède, F. Lu-Hf and PbSL geochronology of apatites from Proterozoic terranes: A first look at Lu-Hf isotopic closure in metamorphic apatite. *Geochim. Cosmochim. Acta* **2005**, *69*, 1847–1859. [[CrossRef](#)]
77. McDowell, F.W.; McIntosh, W.C.; Farley, K.A. A precise  $^{40}\text{Ar}/^{39}\text{Ar}$  reference age for the Durango apatite (U-Th)/He and fission-track dating standard. *Chem. Geol.* **2005**, *214*, 249–263. [[CrossRef](#)]
78. Meffre, S.; Large, R.R.; Scott, R.; Woodhead, J.; Chang, Z.; Gilbert, S.E.; Danyushevsky, L.V.; Maslennikov, V.; Herdt, J.M. Age and pyrite Pb-isotopic composition of the giant Sukhoi Log sediment-hosted gold deposit, Russia. *Geochim. Cosmochim. Acta* **2008**, *72*, 2377–2391. [[CrossRef](#)]
79. Li, Q.L.; Li, X.H.; Wu, F.Y.; Yin, Q.Z.; Ye, H.M.; Liu, Y.; Tang, G.Q.; Zhang, C.L. In-situ SIMS U-Pb dating of phanerozoic apatite with low U and high common Pb. *Gondwana Res.* **2012**, *21*, 745–756. [[CrossRef](#)]
80. Liu, Y.S.; Hu, Z.C.; Gao, S.; Günther, D.; Xu, J.; Gao, C.G.; Chen, H.H. In situ analysis of major and trace elements of anhydrous minerals by LA-ICP-MS without applying an internal standard. *Chem. Geol.* **2008**, *257*, 34–43. [[CrossRef](#)]
81. Scherer, E.; Münker, C.; Mezger, K. Calibration of the Lutetium-Hafnium clock. *Science* **2001**, *293*, 683–687. [[CrossRef](#)]
82. Griffin, W.L.; Belousova, E.A.; Shee, S.R.; Pearson, N.J.; Reilly, Archean crustal evolution in the northern Yilgarn Craton: U-Pb and Hf-isotope evidence from detrital zircons. *Precambrian Res.* **2004**, *131*, 231–282. [[CrossRef](#)]
83. Griffin, W.L.; Wang, X.; Jackson, S.E.; Pearson, N.J.; O'Reilly, S.Y.; Xu, X.S.; Zhou, X.M. Zircon chemistry and magma mixing SE China: In-situ analysis of Hf isotopes, Tonglu and Pingtan igneous complexes. *Lithos* **2002**, *61*, 237–269. [[CrossRef](#)]
84. Rubatto, D. Zircon trace element geochemistry: Partitioning with garnet and the link between U-Pb ages and metamorphism. *Chem. Geol.* **2002**, *184*, 123–138. [[CrossRef](#)]

85. Wu, Y.B.; Zheng, Y.F. Genetic mineralogy of zircons and its constraints on U-Pb age interpretation. *Chin. Sci. Bull.* **2004**, *49*, 1589–1604. (In Chinese) [[CrossRef](#)]
86. Middlemost, E.A. Naming materials in the magma/igneous rock system. *Earth Sci. Rev.* **1994**, *37*, 215–224. [[CrossRef](#)]
87. Sun, S.S.; McDonough, W.F. Chemical and isotopic systematics of oceanic basalts: Implications or mantle composition and processes in so unders AD. In *Magmatism in the Ocean Basins*; Norry, M.J., Ed.; Geological Society Publications: London, UK, 1989; Volume 42, pp. 313–345. [[CrossRef](#)]
88. Du, L.; Zhang, Y.; Huang, Z.; Li, X.P.; Yuan, C.; Wu, B.; Long, X. Devonian to carboniferous tectonic evolution of the Kangguer Ocean in the Eastern Tianshan, NW China: Insights from three episodes of granitoids. *Lithos* **2019**, *350*, 105243. [[CrossRef](#)]
89. Li, X.H.; Li, Z.X.; Li, W.X.; Liu, Y.; Yuan, C.; Wei, G.; Qi, C. U-Pb zircon, geochemical and Sr-Nd-Hf isotopic constraints on age and origin of Jurassic I- and A-type granites from central Guangdong, SE China: A major igneous event in response to foundering of a subducted flat-slab? *Lithos* **2007**, *96*, 186–204. [[CrossRef](#)]
90. King, P.L.; White, A.J.R.; Chappell, B.W.; Allen, C.M. Characterization and origin of aluminous A-type granites from the Lachlan Fold Belt, southeastern Australia. *J. Petrol.* **1997**, *38*, 371–391. [[CrossRef](#)]
91. Chappell, B.W. Aluminium saturation in I- and S-type granites and the characterization of fractionated haplogranites. *Lithos* **1999**, *46*, 535–551. [[CrossRef](#)]
92. Wolf, M.B.; London, D. Apatite dissolution into peraluminous haplogranite melts: An experimental study of solubilities and mechanisms. *Geochim. Cosmochim. Acta* **1994**, *58*, 4127–4145. [[CrossRef](#)]
93. Ding, X.; Su, K.; Yan, H.; Liang, J.; Sun, W. Effect of F-Rich Fluids on the A-Type Magmatism and Related Metal Mobilization: New Insights from the Fogang-Nankunshan-Yajishan Igneous Rocks in Southeast China. *J. Earth Sci.* **2022**, *33*, 591–608. [[CrossRef](#)]
94. Whalen, J.B.; Currie, K.L.; Chappell, B.W. A-type granites: Geochemical characteristics, discrimination and petrogenesis. *Contrib. Mineral. Petr.* **1987**, *95*, 407–419. [[CrossRef](#)]
95. Chung, S.L.; Chun, M.F.; Ji, J.Q. The nature and timing of crustal thickening in Southern Tibet: Geochemical and zircon Hf isotopic constraints from post-collisional adakites. *Tectonophysics* **2009**, *477*, 36–48. [[CrossRef](#)]
96. Gerdes, A.; Montero, P.; Bea, F.; Fershater, G.; Borodina, N.; Osipova, T.; Shardakova, G. Peraluminous granites frequently with mantle-like isotope compositions: The continental-type Murzinka and Dzhabyk batholiths of the eastern Urals. *Int. J. Earth Sci.* **2002**, *91*, 3–193. [[CrossRef](#)]
97. Chappell, B.W.; White, A.J.R. I- and S-type granites in the Lachlan Fold Belt. *Earth Environ. Sci. Trans. R. Soc. Edinb.* **1992**, *83*, 1–26. [[CrossRef](#)]
98. Kemp, A.I.S.; Hawkesworth, C.J.; Foster, G.L.; Paterson, B.A.; Woodhead, J.D.; Hergt, J.M.; Gray, C.M.; Whitehouse, M.J. Magmatic and crustal differentiation history of granitic rocks from Hf-O isotopes in zircon. *Science* **2007**, *315*, 980–983. [[CrossRef](#)]
99. Xiao, B.; Chen, H.Y.; Hollings, P.; Han, J.S.; Wang, Y.F.; Yang, J.T.; Cai, K.D. Magmatic evolution of the Tuwu-Yandong porphyry Cu belt, NW China: Constraints from geochronology, geochemistry and Sr-Nd-Hf isotopes. *Gondwana Res.* **2017**, *43*, 74–91. [[CrossRef](#)]
100. Du, L.; Long, X.; Yuan, C.; Zhang, Y.; Huang, Z.; Wang, X.; Yang, Y. Mantle contribution and tectonic transition in the Aqishan-Yamansu Belt, Eastern Tianshan, NW China: Insights from geochronology and geochemistry of Early Carboniferous to Early Permian felsic intrusions. *Lithos* **2018**, *304–307*, 230–244. [[CrossRef](#)]
101. Sha, L.K.; Chappell, B.W. Apatite chemical composition, determined by electron microprobe and laser-ablation inductively coupled plasma mass spectrometry, as a probe into granite petrogenesis. *Geochim. Cosmochim. Acta* **1999**, *63*, 3861–3881. [[CrossRef](#)]
102. Sun, C.Y.; Cawood, P.A.; Xu, W.L.; Zhang, X.M.; Tang, J.; Li, Y.; Sun, Z.X.; Xu, T. In situ geochemical composition of apatite in granitoids from the eastern Central Asian Orogenic Belt: A window into petrogenesis. *Geochim. Cosmochim. Acta* **2022**, *317*, 552–573. [[CrossRef](#)]
103. Miles, A.J.; Graham, C.M.; Hawkesworth, C.J.; Gillespie, M.R.; Hinton, R.W.; Bromiley, G.D.; EMMAC. Apatite: A new redox proxy for silicic magmas? *Geochim. Cosmochim. Acta* **2014**, *132*, 101–119. [[CrossRef](#)]
104. Zafar, T.; Rehman, H.U.; Mahar, M.A.; Alam, M.; Oyebamiji, A.; Rehman, S.U.; Leng, C.B. A critical review on petrogenetic, metallogenetic and geodynamic implications of granitic rocks exposed in north and east China: New insights from apatite geochemistry. *J. Geodyn.* **2020**, *136*, 101723. [[CrossRef](#)]
105. Harlov, D.E.; Forster, H.J. Fluid-induced nucleation of (Y+REE)-phosphate minerals within apatite: Nature and experiment, Part II. Fluorapatite. *Am. Mineral.* **2003**, *88*, 1209–1229. [[CrossRef](#)]
106. Harlov, D.E.; Wirth, R.; Forster, H.J. An experimental study of dissolution reprecipitation in fluorapatite: Fluid infiltration and the formation of monazite. *Contrib. Mineral. Petrol.* **2005**, *150*, 268–286. [[CrossRef](#)]
107. Harlov, D.E. Apatite: A fingerprint for metasomatic processes. *Elements* **2015**, *11*, 171–176. [[CrossRef](#)]
108. Budzyń, B.; Harlov, D.E.; Williams, M.L.; Jercinovic, M.J. Experimental determination of stability relations between monazite, fluorapatite, allanite, and REE-epidote as a function of pressure, temperature, and fluid composition. *Am. Mineral.* **2011**, *96*, 1547–1567. [[CrossRef](#)]
109. O’Sullivan, G.; Chew, D.; Kenny, G.; Henrichs, I.; Mulligan, D. The trace element composition of apatite and its application to detrital provenance studies. *Earth Sci. Rev.* **2020**, *201*, 103044. [[CrossRef](#)]
110. Muhtar, M.N.; Wu, C.Z.; Brzozowski, M.J.; Zhang, W.F.; Chen, B.Y.; Lei, R.X.; Xiao, W.J. Age and genesis of the Jinshan gold deposit in the Chinese North Tianshan: A link to large-scale strike-slip shearing events. *Ore Geol. Rev.* **2022**, *142*, 104734. [[CrossRef](#)]

111. Xu, X.K.; Li, X.F. Metamorphism of kanggurtag ductile shear zone. *Xinjiang Geol.* **1994**, *12*, 259–264. (In Chinese)
112. Yang, X.K.; Zhang, L.C.; Ji, J.S.; Zeng, Z.R.; Tao, H.X. Analysis of deformation features of Qiugamintashi- Huangshan ductile shear zone, eastern Tianshan. *J. Xi'an Eng. Univ.* **1998**, *20*, 11–18. (In Chinese)
113. Liu, C.P.; Yang, H.M.; Duan, R.C.; Cai, Y.X.; Zhang, C.H.; Zhang, L.G.; Tan, J.J. Metallogenic age of the Matoutan gold deposit in East Tianshan and its geological significance. *Geol. Bull. China* **2014**, *33*, 912–923. (In Chinese)
114. Tang, J.H.; Gu, L.X.; Zhang, Z.Z.; Wu, C.Z.; San, J.Z.; Wang, C.S.; Liu, S.H.; Li, G.R. Peraluminous granite in Huangshan-Jingerquan area of eastern Tianshan: Geochemistry, mineralogy and geochronology. *Acta Petrol. Sin.* **2008**, *24*, 921–946. (In Chinese)
115. Zhou, T.F.; Yuan, F.; Zhang, D.Y.; Fan, Y.; Liu, S.; Peng, M.X.; Zhang, J.D. Geochronology, tectonic setting and mineralization of granitoids in Jueluotage area, eastern Tianshan, Xinjiang. *Acta Petrol. Sin.* **2010**, *26*, 478–502. (In Chinese)
116. Sun, H.S.; Li, H.; Danišík, M.; Xia, Q.L.; Jiang, C.L.; Wu, P.; Yang, H.; Fan, Q.R.; Zhu, D.S. U-Pb and Re-Os geochronology and geochemistry of the Donggebi Mo deposit, Eastern Tianshan, NW China: Insights into mineralization and tectonic setting. *Ore Geol. Rev.* **2017**, *86*, 584–599. [[CrossRef](#)]
117. Han, C.M.; Xiao, W.J.; Zhao, G.C.; Sun, M.; Qu, W.J.; Du, A.D. Re-Os geochronology on molybdenites from the Donggebi Mo deposit in the Eastern Tianshan of the Central Asia Orogenic Belt and its geological significance. *Resour. Geol.* **2014**, *64*, 136–148. [[CrossRef](#)]
118. Zhang, D.; Zhou, T.; Yuan, F.; Xiao, W.; White, N.C.; Deng, Y.F.; Lu, W.; Deng, G. Petrogenesis and mineralization potential of a granite porphyry intrusion beneath the Baishan Mo deposit, Eastern Tianshan, NW China. *J. Asian Earth Sci.* **2015**, *113*, 254–265. [[CrossRef](#)]
119. Stipp, M.; Stünitz, H.; Heilbronner, R.; Schmid, S.M. The eastern Tonale fault zone: A ‘natural laboratory’ for crystal plastic deformation of quartz over a temperature range from 250 to 700 °C. *J. Struct. Geol.* **2002**, *24*, 1861–1884. [[CrossRef](#)]
120. Passchier, C.W.; Trouw, R.A.J. *Microtectonics*, 2nd ed.; Springer: Berlin, Germany, 2005; pp. 1–289.
121. Fossen, H.; Cavalcante, G.C.G. Shear zones—A review. *Earth Sci. Rev.* **2017**, *171*, 434–455. [[CrossRef](#)]
122. Tian, Z.H.; Xiao, W.J.; Sun, J.M.; Windley, B.F.; Glen, R.; Han, C.M.; Zhang, Z.Y.; Zhang, J.E.; Wan, B.; Ao, S.J.; et al. Triassic deformation of Permian Early Triassic arc-related sediments in the Beishan (NW China): Last pulse of the accretionary orogenesis in the southernmost Altaids. *Tectonophysics* **2015**, *662*, 363–384. [[CrossRef](#)]
123. Xiao, W.J.; Song, D.F.; Windley, B.F.; Li, J.L.; Han, C.M.; Wan, B.; Zhang, J.E.; Ao, S.J.; Zhang, Z.Y. Accretionary processes and metallogenesis of the Central Asian Orogenic Belt: Advances and perspectives. *Sci. China Earth Sci.* **2020**, *63*, 329–361. [[CrossRef](#)]